Technische
Universität
München

Ludwig - Maximilians
Universität
München

Max-Planck-Institut
Für
Quantenoptik

Silicon Vacancy Defects in Diamond as Single Photon Source

Master of Science Thesis

Aslı UĞUR

Munich, November-2006

TECHNISCHE UNIVERSITÄT MÜNCHEN

Abstract

For the applications in quantum information and experiments on the foundations of quantum mechanics a robust narrow-band single photon source is desirable. We report on single photon emission from the Silicon Vacancy (SiV) centers in diamond fabricated by ion implantation. Single SiV centers are photostable and have a spectrum consisting of a sharp zero phonon line (FWHM is about 5 nm) at 738 nm and only very weak vibronic sidebands at room temperature. The short luminescence lifetime of 1.2 ns enables an efficient generation of single photons. We employed nitrogen doping to suppress nonradiative transitions of single SiV centers and used a diamond solid immersion lens to improve the collection efficiency of single photons. It is promising to build an efficient single photon source based on the SiV centers.

Contents

Chapter 1

Introduction

After the wave interpretation of diffraction was given by Fresnel in 1815, Maxwell formulated the electro magnetic wave equation in 1873. The wave theory of light was generally accepted at the end of 19th century. The situation changed radically in 1901 with Planck's hypothesis. In 1901, Max Planck derived the spectral distribution of thermal light by postulating that the energy of a harmonic oscillator is quantized, so called quanta. In addition to that A. Einstein showed that the photoelectric effect could be explained by the hypothesis that the energy of a light beam was distributed in discrete packages.

Many optical experiments can be adequately explained using classical theory of electromagnetic radiation based on Maxwell's equations. The first serious attempt to reveal the quantum nature of light was performed by Taylor in 1909. He set up a Young's slit experiment with strongly attenuated light. To his disappointment, he found no noticeable change in the interference pattern, even at very low intensities where less than one photon existed in the apparatus at one time.

The experiment, which studies the intensity correlation of light field, was done firstly by R. Hanbury Brown and R. Q. Twiss and effectively is the birth of the modern quantum optics. In the Hanbury Brown-Twiss experiment the photon bunching was observed for the thermal light [1], which is a consequence of the large intensity fluctuations of thermal sources. This type of photon bunching phenomena may be sufficiently explained both by classical and quantum theory.

The invention of laser changed this situation dramatically. The classical features of laser light are closer to radio waves, that is, it was rather like a

plane wave field. Pioneering work [2] showed that laser light also had a pure quantum aspect which had never been considered before [3].

The quantum theory gives different predictions than its classical counterpart. This was first investigated by R.J. Glauber in his quantum formulation of optical coherence theory [4], [5]. One such prediction is photon antibunching where the initial slope of the intensity correlation function is positive. A classical theory of fluctuating field amplitudes would require negative probabilities in order to give photon antibunching. In the quantum picture it is easly visualized by assuming that photon arrivals one more regularly than Poissonian.

The first antibunching of light, which is generated in resonance fluorescence from a two-level atom, was observed by Kimble *et al.* [6]. In this experiment, an atomic beam is used and hence the photon antibunching was convolved with the atom number fluctuations in the beam.

The development of quantum optics not only provides a deep insight into the nature of light, it contributes also greatly to field of quantum information processing which has been extensively investigated recently.

1.1   Why Single Photons?

There are two branches of modern cryptographic techniques: public-key encryption and secret-key encryption. In public-key cryptography, messages are exchanged using keys that depend on the assumed difficulty of certain mathematical problems [7]. Each participant has a *public key* and a *private key*; the former is used by others to encrypt messages, and the latter by the participant to decrypt them.

In secret-key encryption, a secret key is shared by two users, who use it to transform plaintext inputs to an encoded cipher using a so called one-time pad the security is absolutely guaranteed [7]. The main practical problem with secret-key encryption is determining a secret key.

Quantum mechanics gives promising solution for this problem. One of the best-known principles of quantum mechanics is that it is impossible to do measurements on quantum system without running the risk of changing the state of the system. This assumes the ultimate data security. If information is encoded into several nonorthogonal states of a quantum system, any attempt to get the information by measuring its properties can alter the particular

state, therefore the presence of an eavesdropper will be detected[1]. This idea is the foundation of the growing field generally known as *quantum cryptography* or quantum key distribution [8]. The security of the transmission arises from the fact that single photon is indivisible and its unknown quantum state cannot be copied [9].

The most common **Q**uantum-**K**ey-**D**istribution(QKD) protocol, which has been implemented in experiments over the last years [7], is the BB84 protocol, which uses single photons as information carriers [10][2]. A security analysis for this protocol under realistic system parameters and against individual attacks has been performed [11], [12]. This analysis shows that the performance of a quantum cryptography system, in terms of communication distance and secure communication rate, is determined by the characteristics of the source of single photon, and of the single-photon detectors.

The most important question of QKD is its security. In real quantum cryptography experiments, a single photon source is usually replaced by attenuated laser pulses (i.e., weak coherent states), which occasionally give out more than one photon. This opens up the possibility of sophisticated eavesdropping attacks such as a photon number splitting attack, where Eve stops all single-photon signals and splits multi-photon signals, keeping one copy herself and re-sending the rest to Bob. The security of practical QKD systems has previously been discussed in [13].

Hwang [14] proposed the decoy state method as an important weapon to combat those sophisticated attack: by preparing and testing the transmission properties of some decoy states, Alice and Bob are in a much better position to catch an eavesdropper. Hwang specifically proposed to use a decoy state with an average number of photon of order 1. Hwangs idea was highly innovative.

Quantum information processing requires indistinguishable photons, identical in frequency and without a phase jump, so they can interfere with each other. And the light source should be efficient, emitting a photon in a large fraction of the possible time slots [15].

Single-photon source research is now focused on developing true single-photon sources that are suitable for different practical applications. The

---

[1]see www.laserfocusworld.com/articles/255503

[2]C.H. Bennett and G. Brassard proposed BB84, the first quantum cryptography protocol, in 1984, but it was not until 1991 that the first experimental prototype based on this protocol was made operable over a distance of 32 centimeters.

main goals are:

- High efficiency, which can be explained by the fraction of time slots occupied by single photons, which is also proportional to the probability the time slot will contain two or more photons instead of one.

- Generation of photons that are indistinguishable from each other.

- High repetition rates and a design that easily couples photons into a transmission fiber or free space. Current efforts are aimed at confining a light-emitting species-as a gas or solid-inside an optical cavity that helps control and couple emission.

1.2   Sources of Single Photons

Any bright light source can be attenuated so that, on average, one photon arrives at a detector in a specific time interval. However, for a classical light source, the number of photons will sometimes be zero, two, or more; it is only the mean value that equals one. The smallest uncertainty in the photon number for a classical light source is achieved with a Poissonian distribution. A typical stream of classical light pulses is illustrated in figure 1.1;

In recent years a variety of implementations for single photon sources have been investigated. Among them are schemes based on single molecules or atoms [16], [17], [18], single ions trapped in cavities [19], color centers in diamonds [20], [21], quantum dots [22], [23] and parametric down conversion (PDC) [24], [25]. These sources differ in the wavelength and purity of the emitted photons, their repetition rate and whether they produce a photon on demand or heralded, i.e, announced by an event. The latter is for example the case with PDC-sources. PDC produces randomly photon pairs and the presence of one photon is indicated by the detection of the other.

In 1977 the first experiment on single photon was done by Kimble *et al.*. The sodium atoms were continously excited by a dye-laser beam and the fluorescence was collected from the atoms at a right angle to both the laser and atomic beams. They produced of antibunched photons and measured resonance of the fluorescence from sodium atoms [6]. The sodium atoms enter the interaction region randomly, thus the single photon emission is convolved by Poissonian distribution of atoms. Afterwords a single ion was hold inside a
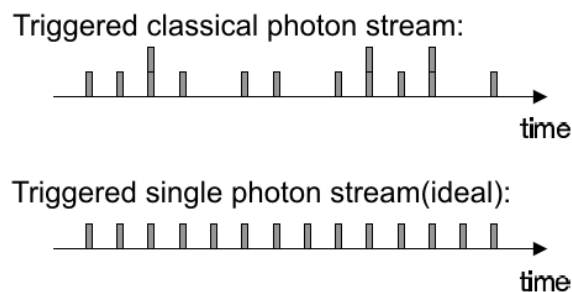
Figure 1.1: A pulsed classical source (top), and a pulsed single-photon source (bottom)

Paul-Trap and laser cooling was used. Considerable efforts were undertaken to reduce its motion before measuring the resonance flouresence [26].
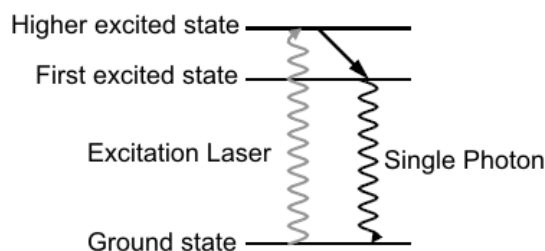
Figure 1.2: Typical optical excitation scheme for a single-photon source. A single quantum system is raised from its ground state to a higher excited state by a laser pulse, relaxes nonradiatively to a lower excited state, and emits a photon through spontaneous emission

The experiments done with these set-ups are not easy to be used in practical applications. Several recent experiments employed quantum dots, organic molecules and colour centers. In such systems, optical excitation is accomplished by focusing a laser pulse onto the quantum system. These systems usually have at least three levels as shown in figure 1.2, so that the laser does not have to be tuned to the same wavelength as the emitted photon. Otherwise, separating the emitted single photon from the scattered laser light (typically 10^8 photons) is difficult. For quantum dots, which have very high

quantum efficiency, to produce a triggered stream of single photons, pulsed excitation can be used [27], [28], [29]. There is no shelving or photobleaching problem in these sources. That material would be compatible with semiconductor technologies, allowing the sources to be incorporated into larger structures. The quantum dots have some problems with collection of the photons which do not leave this high refractive index material. Improvement of collection efficiency is needed. As a solution microcavities can be used. If a QD is in resonance with the cavity mode, the spontenous emission goes mainly into cavity mode, and the spontaneous emission rate can be enhanced [30].

Single organic molecules were incorparated in a crystalline host as dilute impurities. By collecting light from a small volume of the sample, luminescence from these molecules can be isolated spatially and also selected spectrally by filtering out the narrow zero phonon line of one molecule luminescence. The antibunching measurement were done on the flourecence of single organic molecules. It has been detected at low temperature [31] and room-temperature [32]. But there is a disadvantage of these molecules. They stop emitting light after some active time, which is known as *photobleaching*.

Nitrogen vacancay centers in synthetic diamond crystals have also been used. NV centers are formed by a substitutional nitrogen atom with a vacancy trapped at an adjacent lattice position. The light emission from NV centers has high quantum efficiency. They do not have any photobleaching effect. Antibunching at room temperature was observed [20], [33]. The disadvantage of this center is the shelving in metastable levels. They stop emmiting light if they are in the metastable level. Another problem is that the light emitted has a wide spectrum.

In this thesis, we have studied Si-V centers in dimaond. The high photostability and the narrow emission bandwidth of about 5 nm at room temperature make SiV centres interesting as a single photon source in practical quantum cryptography. We have used a diamond **S**olid-**I**mmesion-**L**ens(SIL) to improve collection efficiency.

1.3   Outline

This thesis will detail our work on using Si-V centers as single photon source and on improving collection efficiency by using a SIL. Chapter 1 and 2 represent the introduction and the background information and form a starting

point for the rest of my thesis, while chapter 3 contains the properties of diamond used in experiments. Chapter 4 explains the experimental techniques which we have been used for investigating the colour centers. Finally, the experimental results are presented in chapter 5.

Chapter 2

Quantum Optics Toolbox

2.1 Photon Counting Statistics

The average photon number detected in a certain time is determined by the
intensity of the light beam, but the fluctuation in the count rate is governed by the statistical properties of the incoming photon stream. There
are three different types of photon statistics; Poissonian, super-Poissonian,
and sub-Poissonian. Poissonian and super-Poissonian statistics in photodetection experiments is consistent with the classical theory of light, but not
sub-Poissonian statistics.

The basic function of the experiment investigating photon statistics is to
count the number of photons that strike the detector in a user-specified time
interval T. In the quantum picture of light, a light beam can be considered as
a stream of photons. The **photon flux** Φ is defined as the average number
of photons passing through a cross section of the beam in unit time. Φ can
be calculated by dividing the energy flux **I** by the energy of the individual
photons:

$$\Phi = \frac{IA}{\hbar\omega} = \frac{P}{\hbar\omega} \quad , \tag{2.1}$$

where A is the area of the beam and P is the power.

Photon counting detectors are specified by their quantum efficiency η,
which is defined as the ratio of the number of photocounts to the number of
incident photons. The average number of counts registered by the detector
in a counting time T is thus given by:

$$N(T) = \eta\Phi T = \frac{\eta P T}{\hbar\omega} \quad . \tag{2.2}$$

The corresponding average **count rate R** is given by:

$$R = \frac{N}{T} = \eta\Phi = \frac{\eta P}{\hbar\omega} \quad . \tag{2.3}$$

The maximum photon counting rate that can be registered with a photon counting system is usually determined by the fact that the detectors need a certain amount of time to recover after each detection event. A 'dead time' must elapse between successive counts. This sets a practical upper limit on R of around $10^6 counts/sec$.

2.1.1 Coherent Light: Poissonian Photon Statistics

In classical physics, light is considered to be an electromagnetic wave. A perfectly coherent light beam which has constant angular frequency ω, phase φ, and amplitude ε_0 can be descirbed as follows:

$$\varepsilon(x,t) = \varepsilon_0 \sin(kx - \omega t + \varphi) \quad , \tag{2.4}$$

where $\varepsilon(x,t)$ is the electric field of the light wave and $k = \frac{\omega}{c}$ in free space. Intensity, I, of the beam is proportional to the square of the electric field, and is constant if ε_0 and φ are time independent, which means that the average photo flux is constant in time. Such a field can be approximated by a laser field. Consider a light beam of constant photon flux Φ. The average number of photons within a beam segment of length L is given by:

$$\bar{n} = \frac{\Phi L}{c} \quad . \tag{2.5}$$

We assume that L is large enough that $\bar{n}$ takes a well-defined integer value. We now subdivide the beam segment into N subsegments of length L/N. N is assumed to be sufficiently large that $\frac{\bar{n}}{N} << 1$.

"What is the probability $P(n)$ of finding n photons within a beam of length L containing N subsegments?"
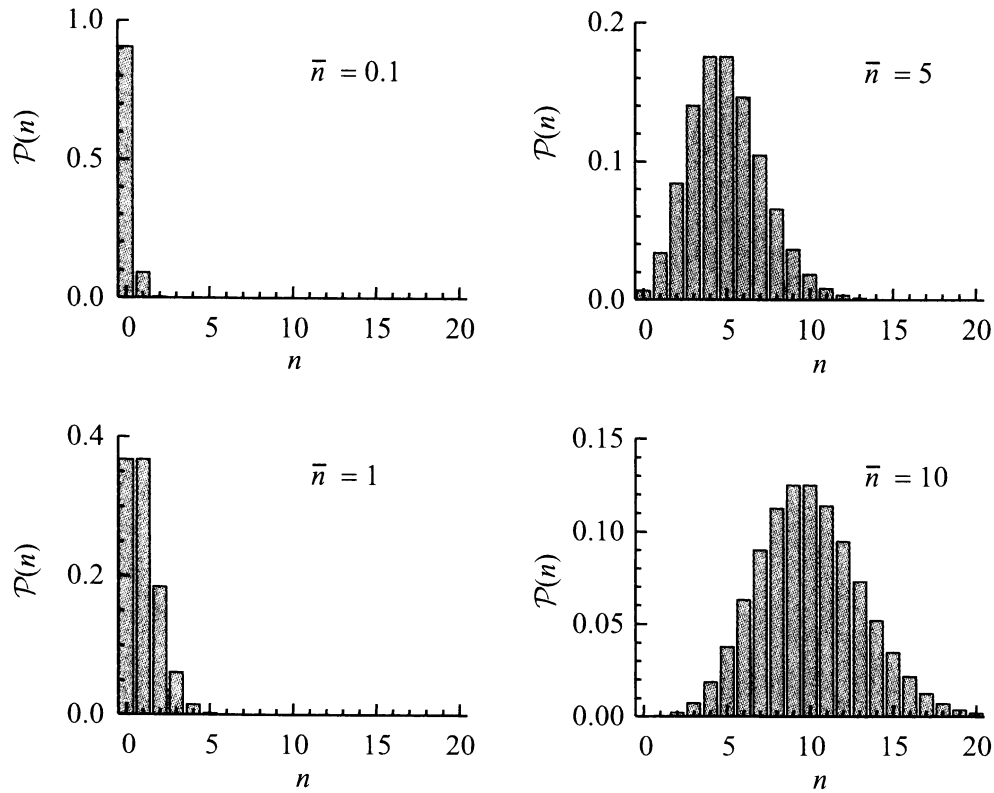
Figure 2.1: Poissonian distributions for mean value *0.1, 1, 5,* and *10.*

The answer is given by some mathematical derivations and is known as Poissonian distribution

$$P(n) = \frac{\bar{n}^n}{n!} e^{-\bar{n}}, n = 0, 1, 2... \quad . \tag{2.6}$$

The Poissonian statistics can be applied to the count rate of a photon-counting system detecting individual photons from a light beam with a constant intensity. In this case the randomness originates from chopping the continuous beam into discrete energy packets with an equal probability of finding the energy packet within any given time subinterval.

Poissonian distributions are uniquely characterized by their mean value $\bar{n}$. Representative distributions for $\bar{n}$=0.1, 1, 5 and 10 are shown in figure 2.1. It is apparent that the distribution peaks close to $\bar{n}$ and gets broader as $\bar{n}$

increases. Fluctuations of a statistical distribution about its mean value are usually quantified in terms of *variance*. The variance is equal to the square of the standard deviation Δn. And is the defined by:

$$Var(n) = (\Delta n)^2 = \sum_{n=0}^{\infty} (n - \bar{n})^2 P(n) \quad . \tag{2.7}$$

It is a well known result for Poissonian statistics that the variance is equal to the mean value $\bar{n}$:

$$(\Delta n)^2 = \bar{n} \quad . \tag{2.8}$$

The standard deviation for the fluctuation of the photon number is therefore given by:

$$\Delta n = \sqrt{\bar{n}} \quad . \tag{2.9}$$

This makes clear that the ratio between standart deviation and the mean value decreases as $\bar{n}$ gets larger.

2.1.2 Classification of Light by Photon Statistics

From a classical perspective, a perfectly coherent beam of constant intensity is the most stable type of light that can be predicted. This therefore provides a bench mark for classifying other types of light according to the standard deviation of their photon number distributions. In general, there are three possibilities

- Sub-Poissonian Statistics:$\Delta n < \sqrt{\bar{n}}$,

- Poissonian Statistics:$\Delta n = \sqrt{\bar{n}}$,

- Super-Poissonian Statistics:$\Delta n > \sqrt{\bar{n}}$,

where $\bar{n}$ and Δn are mean value and standard deviation, respectively.

The difference between the three different types of statistics is illustrated in figure 2.2. In this figure, the photon number distributions of Super-Poissonian and Sub-Poissonian light are compared to that of a Poissonian
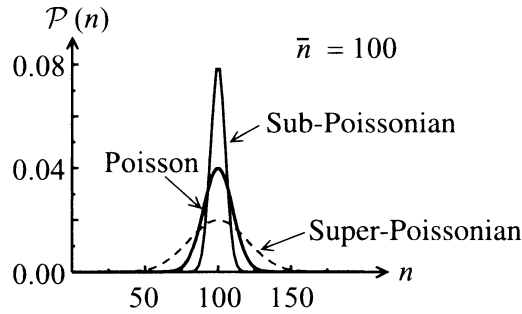
Figure 2.2: Comparison of the photon statistics for light. The distributions have been drawn with the same mean photon number.

distribution with the same mean photon number. We see that distributions of Super-Poissonian and Sub-Poissonian light are, respectively, broader or narrower than Poisson distribution.

If there are any classical fluctuations in the intensity, then we would expect to observe large photon number fluctuations than for the case of perfectly coherent beam. Since perfectly coherent beam obeys Poissonian statistics, it follows that all classical light beams with time-varying intensities will have Super-Poissonian photon number distribution.

Sub-Poissonian light, by contrast, has a narrower distribution than the Poissonian case and is therefore 'quiter' than perfectly coherent light. Now we have already emphasized that a perfectly coherent beam is the stablest form of light that can be envisaged in classical optics. It is therefore apparent that Sub-Poissonian light has no classical counterpart, and is therefore an example of non-classical light.

Super-Poissonian Light

Super-Poissonian light is defined by the relation: $\Delta n > \sqrt{\bar{n}}$. Super-Poissonian statistics has a classical interpretation in terms of fluctuations in the light intensity. A real light source has certain unstability in intensity, and therefore the observation of Super-Poissonian statistics is common place.

Chaotic light is an example of Super-Poissonian Statistics. The light from a discharge lamp is generally called chaotic light. Chaotic light has partial coherence; with classical intensity fluctuations on a time scale determined by

the coherence time τ_c.

Figure 2.7 shows a computer simulation of the time dependence of the intensity of the light emitted by a chaotic source with a coherence time of τ_c. It can be supposed that each atom emits at the same frequency , but due to random collision the phase of the light from the individual atoms is constantly changing. The summation of the randomly phased light from the millions of light emitting atoms in the source causes the fluctuations. As we can see from the graph the intensity fluctuates above and below the average value $\langle I \rangle$ widely comparable to τ_c.

Sub-Poissonian Light

Sub-Poissonian light is defined by the relation: $\Delta n < \sqrt{\bar{n}}$. Sub-Poissonian light has a smaller photon number uncertainty than Poissonian statistics. A perfectly coherent beam with constant intensity has Poissonian photon statistics. We thus conclude that Sub-Poissonian light is more stable than perfectly coherent light. Sub-Poissonian light has no classical equivalent. Therefore, the observation of Sub-Poissonian statistics is a clear signature of the quantum nature of light. Let us consider the properties of a beam of light in which time intervals Δt between the photons are identical, as illustrated schematically in figure 2.3(a). The photo-count obtained for such a beam in a time T would be integer value determined by:

$$N = Int(\eta \frac{T}{\Delta t}) \quad , \tag{2.10}$$

which would be exactly the same for every measurement. The experimenter would therefore obtain the histogram shown in figure 2.3(b), with $\bar{n} = N$ given by equation (2.10). This is highly sub-Poissonian, and has $\Delta n = 0$.

Photon streams of the type shown in figure 2.3(a) with $\Delta n = 0$ are called photon number states. Other types of sub-Poissonian light can be conceived in which the time intervals between the photons in the beam are not exactly the same, but are still more regular than the random time intervals appropriate to a beam with Poissonian statistics.
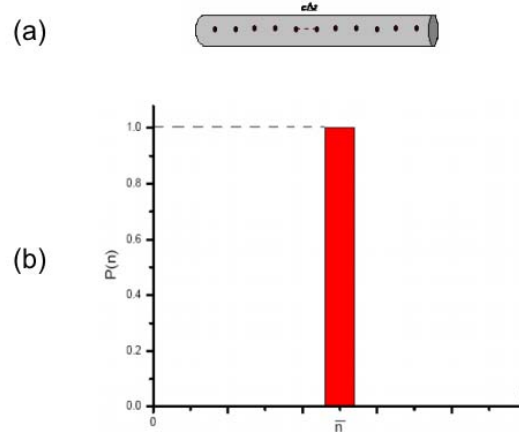
Figure 2.3: (a) Beam of light containing a stream of photons with a fixed-time spacing Δt between them. (b) Photon counting statistics for such a beam.

2.2   The second order correlation function

"How can we quantify how good a single photon source is?" Normalized second order correlation is a function which can be used to answer this question. It can be written as:

$$g^{(2)} = \frac{\langle \varepsilon^*(t)\varepsilon^*(t+\tau)\varepsilon(t+\tau)\varepsilon(t)\rangle}{\langle \varepsilon^*(t)\varepsilon(t)\rangle\langle \varepsilon^*(t+\tau)\varepsilon(t+\tau)\rangle} = \frac{\langle I(t)I(t+\tau)\rangle}{\langle I(t)\rangle\langle I(t+\tau)\rangle} \quad , \qquad (2.11)$$

where $\varepsilon(t)$ and $I(t)$ are the electric field amplitudes and intensity of the light beam at time t. The $\langle \cdots \rangle$ indicates the time average computed by integrating over a long time period. Such that, $\langle I(t)\rangle = \langle I(t+\tau)\rangle$ for a source which has a constant average intensity.

First of all, we need the second order correlation function to analyse the results that we have derived classiccally in terms of intensity fluctuations. We assume that we are testing spatially coherent light from a small area of the source. In these conditions the second order correlation function investigates the temporal coherence of the source.

The time scale of the intensity fluctuations is determined by the coherence time τ_c of the source. The intensity fluctuations at times t and $t+\tau$ will be completely uncorrelated with each other , if $t \gg \tau_c$. The time dependent intensity can be written as:

$$I(t) = \langle I \rangle + \Delta I(t) \tag{2.12}$$

with $\langle \Delta I(t) \rangle = 0$, we than have from equation (2.21) that:

$$\langle I(t)I(t+\tau) \rangle_{\tau \gg \tau_c} = \langle I \rangle^2 \quad . \tag{2.13}$$

Therefore;

$$g^{(2)}(\tau \gg \tau_c) = \frac{\langle I(t)I(t+\tau) \rangle}{\langle I(t) \rangle^2} = 1 \quad . \tag{2.14}$$

On the other hand for the case $\tau \ll \tau_c$, there will be correlations between the fluctuations at the two times. If $\tau = 0$, we have;

$$g^{(2)}(0) = \frac{\langle I(t)^2 \rangle}{\langle I(t) \rangle^2} \quad . \tag{2.15}$$

For any conceivable time dependence of $I(t)$, it will always be the case that

$$g^{(2)}(0) \geq 1 \tag{2.16}$$

and

$$g^{(2)}(0) \geq g^{(2)}(\tau) \quad . \tag{2.17}$$

We can give an explanation of the validity if the inequality above. First ,we can consider a perfectly coherent monochromatic source which has a time independent intensity I_0. In this case, it is clear that $g^{(2)}(\tau) = 1$ for all values of τ since I_0 is constant. Finally we can consider any source which has a time varying intensity. Because there are intensity fluctuations above and below the average, $\langle I(t)^2 \rangle \geq \langle I(t) \rangle^2$ and the squaring process exaggerates the fluctuations above the mean value. Putting all these arguments together, it can be realized that, we expect $g^{(2)}(\tau)$ to decrease with τ, for any source with a time varying intensity, reaching the value of unity for large τ. We expect a constant value of $g^{(2)}(\tau) = 1$ in the special case where $I(t)$ does not vary with time. It can be seen that these conclusion are in agrement with equation (2.16) and (2.17).

Light Source	Property	Comment
Classical light	$\begin{cases} \mathrm{g}^{(2)}(0) \geq 1 \\ \mathrm{g}^{(2)}(0) \geq g^{(2)}(\tau) \end{cases}$	$\mathrm{g}^{(2)}(0) = 1$ when $I(t) = const.$
Perfectly coherent light	$g^{(2)}(\tau) = 1$	Applies for all τ
Gaussian chaotic light	$g^{(2)}(\tau) = 1 + e^{-\pi(\frac{\tau}{\tau_c})^2}$	τ_c =coherence time
Lorentzian chaotic light	$g^{(2)}(\tau) = 1 + e^{-2\frac{|\tau|}{\tau_0}}$	τ_0 =lifetime

Table 2.1: Properties of the second order correlation function for classical light

It is instructive to considered the explicit forms of the second order correlation function for the various forms of light that we usually consider in clasical optics. We already know that perfectly coherent light has $g^{(2)}(\tau) = 1$ for all τ. The values of $g^{(2)}(\tau)$ for the chaotic light from an atomic discharge lamp can be calculated by assuming simple models of the source. The second order correlation functions for different types of light are given by in table below:

We have classified light according to whether the statistics were sub-Poissonian, Poissonian, or super-Poissonian. We now make a different three-fold classification according to the second order correlation function $g^{(2)}(\tau)$. This classification is based on the value of $g^{(2)}(0)$ and proceeds as follows:

Classical decription	Photon stream	$g^{(2)}(0)$
Chaotic	Bunched	> 1
Coherent	Random	1
None	Antibunched	< 1

Table 2.2: Classification of light according to the photon time intervals. Antibunched light is a purely quantum state with no classical equivalent. classical light must have $g^{(2)}(0) \geq 1$.

If we compare the properties of light of table **??** and 2.2 we can realize that bunched and coherent light are compatible with the classical results, but antibunched light not. Antibunched light has no classical counterpart and is thus a purely quantum optical phenomenon. Simply we can illustrate the difference between the three different types of light in terms of the photon streams. This is shown in figure 2.4;
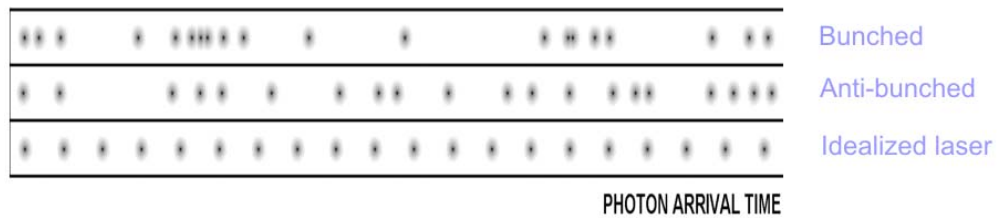
Figure 2.4: Statistics of photon arrival times in light beams with different entropies (different degrees or *ordering*). The statistics can be *quantum-random*, as in maximum-entropy black-body radiation (following a Bose-Einstein distribution with a certain *bunching* in time; top), or may be quite different if the radiation deviates from thermodynamic equilibrium, e.g. for anti-bunched photons (where photons tend to avoid one another; center), or a uniform photon density as in stimulated emission from an idealized laser (bottom). The characteristic fluctuation timescales are those of the ordinary [first-order] coherence time of light, fully developed on extremely short timescales (of order picoseconds for a 1 nm passband of optical light.), but traces of which are detectable also with slower, experimentally realistic time resolutions [34].

In the middle is the case where the time intervals between the photons are random. Below it we have the case were the photons spread out with regular time intervals between them, and above it where they clump together in bunches. These three cases correpond to coherent, antibunched and bunched light, respectively. Now we will discuss these three type of light in more detail.

2.2.1   Coherent light

Perfectly coherent light has $g^{(2)}(\tau) = 1$ for all values of τ including $\tau = 0$. It thus provides a convenient reference for classifying other types of light.

Perfectly coherent light has Poissonian photon statistics, with random time intervals between photons. It implies that the probability of detection of a photon is the same for all values of τ independent of any previous emission. We can thus say that coherent light has $g^{(2)}(\tau) = 1$ for all values of τ as a manifestation of the randomness of the Poissonian photon statistics.

2.2.2   Bunched light

Bunched light [1] is defined as light with $g^{(2)}(0) > 1$. It consists of a stream of photons with the photons all clumped together in bunches. This means that if we detect a photon at time $t = 0$, there is a higher probability of detecting another photon in short times than in long times. Hence we expect $g^{(2)}(\tau)$ to be larger for small values of τ than for bigger ones, so that $g^{(2)}(\tau) > g^{(2)}(\infty)$.

As we have seen before classical light must satisfy the conditions equation (2.16) and (2.17). It is clear that bunched light satisfies these conditions and is therefore consistent with classical interpretation. And from table **??** it is also clear that cahotic light(whether Gaussian or Lorentzian) also satisfies these conditions. The chaotic light from a discharge lamp is therefore bunched.

2.2.3   Antibunched light

In antibunched light the photons come out with regular gaps between them, rather than with random spacing. If the flow of photons is regular, then

---

[1] *The tendency for photons to bunche together may be considered to be a manifestation of the fact that they are bosons.*

there will be long time intervals between observing photon counting events. In this case, the probability of detection of second photon after one photon is detected is small for small values of τ and then increases with τ. Antibunched light has:

$$\begin{aligned} g^{(2)}(0) &< g^{(2)}(\tau) \quad , \\ g^{(2)}(0) &< 1 \quad . \end{aligned} \qquad (2.18)$$

This is not in agrement with equation (2.16) and (2.17) which apply to classical light. It is apparent that observation of photon antibunching is purely quantum effect with no classical counterpart. The sub-poissonian light, like antibunched light, is also a clear signature of the quantum nature of light. Here we can think about; whether photon antibunching and sub-Poissonian photon statistics are different manifestations of the same quantum optical phenomenon. Thus although the two phenomena are not identical, it will frequently be the case that non-classical light will show both photon antibunching and sub-Poissonian photon statistics at the same time.

2.3 Optical Hanbury Brown and Twiss Experiment

Hanbury Brown and Twiss were two astronomers. They aimed to measure the diameters of stars. For this purpose they developed the intesnsity interferometer. They observed for the first time correlations between identical particles [1]. Their idea was that intensity fluctuations and the resulting correlations reveal information about the coherence and the quantum statistics of the probed system. This principle has found applications in many fields of physics such as astronomy, high-energy physics [35], atomic physics [36] and condensed matter physics [37], [38].

They tested the principle of their experiment in the labrotory with a simple set up. A schematic representation of the setup is shown in figure 2.6

A half silvered mirror was used to split 435.8 nm line from a mercury discharge lamp. This light was detected by two photomultipliers. These photomultipliers generated photocurrents I_1 and I_2. An AC-coupled amplifier was used to feed these photocurrents. In this way they got the outputs proportional to fluctuations in the photocurrents, Δi_1 and Δi_2. One of these
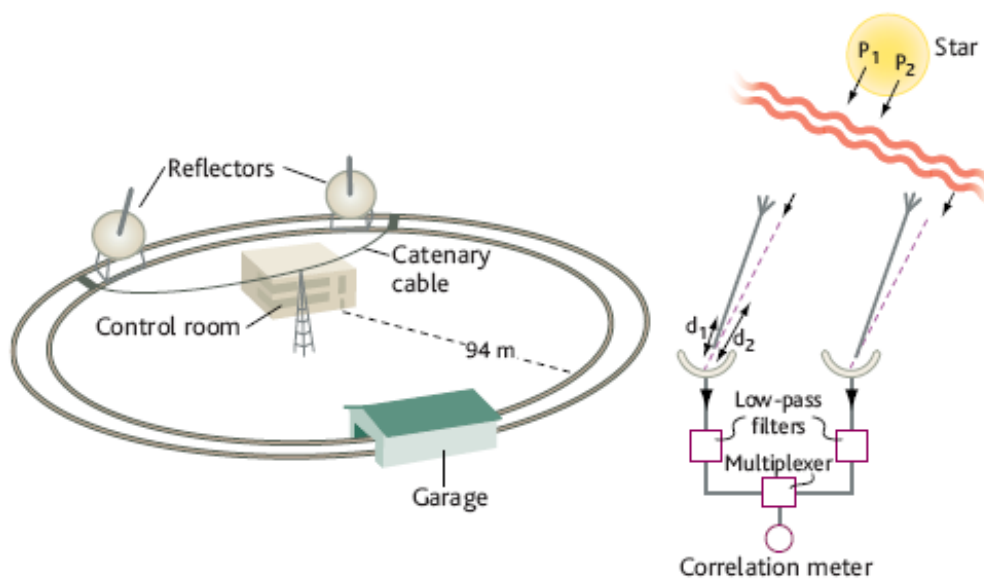
Figure 2.5: Coherence in light and matter; (Left) Sketch of the intensity interferometer used by Hanbury Brown and Twiss to measure the fluctuations in light from stars to deduce stellar sizes. (Right) Schematic of the Hanbury Brown and Twiss measurement of the correlations observed at two points from an extended optical source such as a star [39].
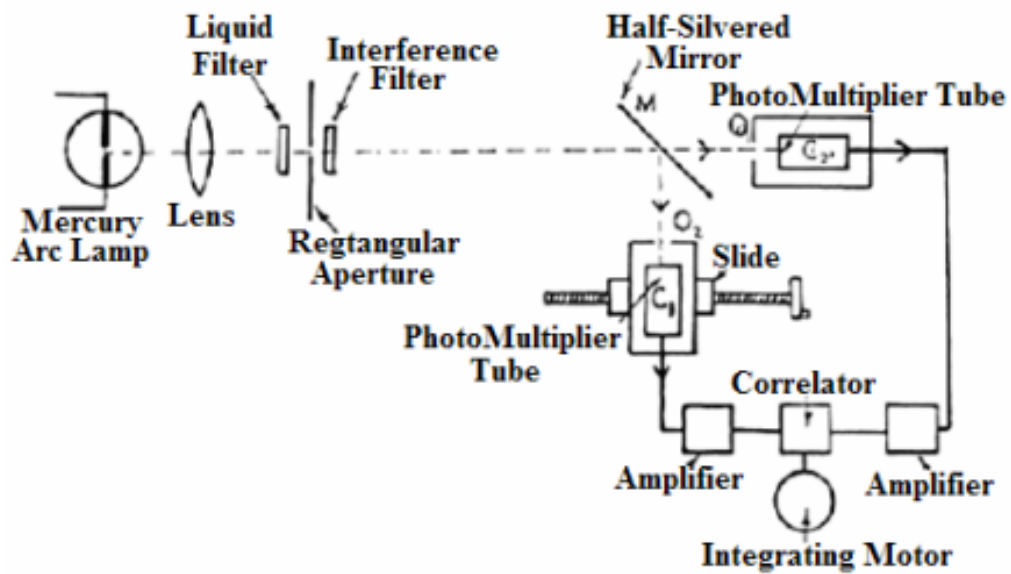
Figure 2.6: Schematic representation of the Hanbury Brown-Twiss (HBT) intensity correlation experiment. Q1 was placed on a translation stages, so that the two detectors could register light separated by a distance d. In this way the spatial coherence of the source could be investigate. (After R. Hanbury Brown and R. Q. Twiss [1].
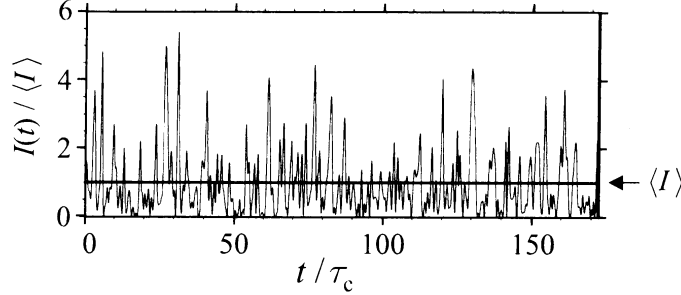
Figure 2.7: The computer generated time series (in units of the coherence time τ_c)for the cyle averaged intensity of Gaussian distributed light, assuming a light source with a Gaussian spectral profile [40].

was passed throug an electronic time delay generator set to a value τ. At last, multiplier-integrator was used to connect two signals to multiply them together and avarage them over a long time. The output signal was proportional to $\langle \Delta i_1(t) \Delta i_2(t + \tau) \rangle$, where $\langle \cdots \rangle$ indicates the time average, where I_1 and I_2 were the light intensities incident on the respective detectors , and Δi_1 and Δi_2 were their fluctuations. The reason for this proportionality is that the photocurrents were proportional to the impinging light intensities.

The intensity fluctuations of a beam of light are related to its coherence. So, we can deduce the coherence properties of light by measuring the correlations of the intensity fluctuations. In the HBT setup the beam splitter is adjusted so that the average intensity $\langle I(t) \rangle$ impinging on the detector is identical. Clasically, we can write the time varying light intensity on the detectors as:

$$I_1(t) = I_2(t) \equiv I(t) = \langle I \rangle + \Delta I(t) \quad , \tag{2.19}$$

where $\Delta I(t)$ is the fluctuation from the mean intensity $\langle I \rangle$. With identical intensities on the detectors the output of the HBT experiment is proportional to $\langle \Delta i_1(t) \Delta i_2(t + \tau) \rangle$.

If we suppose that the time delay τ is zero, we have the output:

$$\langle \Delta I(t) \Delta I(t + \tau) \rangle_{\tau=0} = \langle \Delta I(t)^2 \rangle \quad . \tag{2.20}$$

Hence there will be a non zero output for $\tau = 0$. On the other hand, if we make $\tau >> \tau_c$, the intensity fluctuations will be completely uncorrelated with each other so that $\Delta I(t)\Delta I(t+\tau)$ randomly changes sign with time and averages to zero:

$$\langle \Delta I(t)\Delta I(t+\tau)\rangle_{\tau>>\tau_c} = 0 \quad . \tag{2.21}$$

The output therefore falls to zero for values of $\tau >> \tau_c$. Hence by measuring the output function as a function of τ we can determine coherence time τ_c directly.

Now we will re-examine the HBT experiments in the quantum picture of light. In figure 2.8 (a) we can see the experimental arrangement for a HBT configured with single photon counting detectors. A stream of photons is incident on a $50 : 50$ beam splitter and is divided equally between the two output ports. The photons coming to the detectors and the resulting output pulses are fed into an electronic counter/timer. The counter/timer records the time elapses between the pulses from D1 and D2, while simultaneously counting the number of pulses at each input. The results of the experiment can be shown as a histogram as in figure 2.8 (b). The histogram displays the number of events that are registered at each value of the time τ between the start and stop pulses.

We discussed $g^{(2)}(\tau)$ function classically in terms of intensity correlations before. Since the number of counts registered on a photon-counting detector is proportional to the intensity, so we can write the second order correlation function for classical light again as:

$$g^{(2)} = \frac{\langle n_1(t)n_2(t+\tau)\rangle}{\langle n_1(t)\rangle \langle n_2(t+\tau)\rangle} \quad , \tag{2.22}$$

where $n_i(t)$ is the number of counts registered on detector i at time t. If the statistical prperties of the light beam being assumed stationary, the correlation now depends on the time τ (with exception of multimode coherent light where the degree of second order coherence is constant as in table 2.1). Thus for multimode chaotic light with a Lorentzian frequency distribution equation (2.22) gives:

$$g^{(2)} = \frac{\langle n_1(0)n_2(\tau)\rangle}{\bar{n_1}\bar{n_2}} = e^{-2\gamma|\tau|} + 1 \quad , \tag{2.23}$$
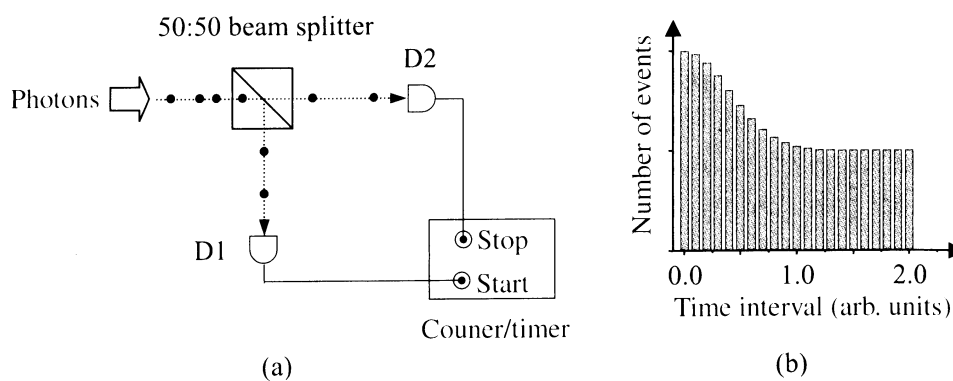
Figure 2.8: *(a)* Sketch of a Hanbury Brown-Twiss (HBT) experiment (with a photon stream incident on the beam splitter. The pulses from the single-photon counting detectors D1 and D2 are fed into the start and stop inputs of an electronic counter/timer both counts the number of pulses from each detectors and also records the time that elapses between the pulses at the start and stop inputs.) *(b)* Typical results of such an experiment. The results are presented as a histogram showing the number of events recorded within a particular time interval. In this case the histogram shows the results that would be obtained for a bunched photon stream.

where γ is the total radiative damping parameter [34]. The first experiment [4] to measure photon-number correlations was made with apparatus similar to that shown in figure 2.8. If the photodetectors are placed at equal linear distances from the source, the HBT correlation obtained from equation (2.24) is

$$g^{(2)} - 1 = e^{-2\gamma|t_2 - t_1|} \quad , \tag{2.24}$$

where the times t_1 and t_2 of the readings are seperated by an amount of τ. As in classical theory of the analogous intensity correlation experiment described in previous part, it is necessary to allow for the finite response time τ_r of the detectors. The experiment registered as correlations, photons that arrived at detector 1 within a time interval τ_r of a photon arrival at detector 2. This is what the histogram from HBT experiment with photon counting detectors records. The result of a HBT experiment gives direct measure of the second order correlation function $g^{(2)}(\tau)$.

We can see from figure 2.8 that compeley different results are possible with photons at the input port of the beam splitter than with a classical electromegnetic wave. We suppose the incoming light consists of a stream of photons, and this light has long time intervals between succesive photons. These photons impinge one by one and randomly to the detectors D1 or D2 with equal probability. So we can say that there is 50% probability that D1 can detect a photon and trigger the timer to start recording. When this photon generates the start pulse, we can be sure that there is a zero probability of obtaining a stop pulse from D2, because second photon arrives after some time interval. Hence at $\tau = 0$ the timer will record no evets. Now let us consider the next photon that impinges on the beam splitter. This photon will also go to detector D2 with 50% probability. If it really goes to D2, it will stop the timer and record an event. If it goes to D1 then nothing happens and we have to wait again until the next photon arrives to get a chance of having a stop pulse. The process takes place until a stop pulse is achieved. This might happen with the first or second or any subsequent photon, but never at $\tau = 0$. Therefore we have a situation where we expect no events at $\tau = 0$, but some events for larger values of τ, which clearly contravenes the classical result given in equation (2.16) and (2.17). We can clearly see that experiments in quantum context can give results that are not possible in the classical theory of light.

The observation of the non-classical result with $g^{(2)}(0) = 0$ arose from the fact that the photon stream consisted of individual photons with definite, non zero time intervals between them. Now let us consider a different case where the photons arrive in bunches. Half of the photons are splited towards D1 and the other half towards D2. These two subdivided bunches strike the detectors at the same time and there will be a high probability that both detectors register simultaneously. Therefore, there will be a large number of events near $\tau = 0$. As τ increases the probability of getting a stop pulse after a start pulse has been registered decreases, and so the number of events recorded drops. As a result we have a situation with many events near $\tau = 0$ and fewer at later times, which is fully compatible with the classical results in equation (2.16) and (2.17).

Sometimes the photon picture concurs with the classical results and sometimes it does not. The key point is the time intervals between the photons in the light beam; that is, whether the photon come in bunches or whether they are regularly spread out. This leads us to the concepts of bunched and antibunched light.

2.3.1 Experimental demonstration

The observation of antibunching is a clear proof of the quantum nature of light. The first succesful demonstration of photon antibunching was using [6] the light emitted by sodium atoms. The basic principle of an antibunching experiment is to isolate an individual quantum emitter (i.e. an individual atom, molecule, quantum dot, or colour center). This was done by focusing a laser onto the fluorescent species to excite them, and then waiting for the photon to be emitted through spontaneous decay. Once a photon has been emitted, the quantum emitter must be excited again to be able to emit another photon. It will take a time dependent on excitation rate and the radiative lifetime of the transition, τ_R, before the next photon can be emitted. This causes time gaps between the photons, and as a result we have antibunched light.

To understand better we can refer to figure 2.9. This figure is a schematic representation of the photon emission sequence from a single atom.

Suppose that the atom is excited at time $t = 0$, as shown by dashed line. Acording to emission probability of the transition, the average time to emit a photon is equal to τ_R. Once a photon has been emitted, the atom can be re-
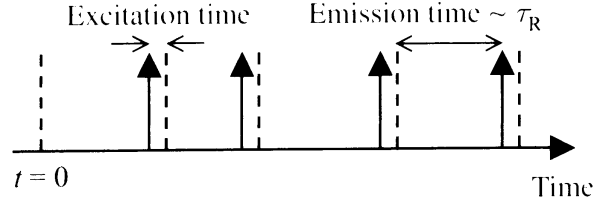
Figure 2.9: Schematic representation of the photon emission sequence from a single atom excited by an intense laser. The dashed lines indicate the times at which the atom is promote to the excited state, while the arrows indicate the photon emission events. τ_R is the radiative lifetime of the excited state.

excited by the laser, which will only require a short time, which is determined by the excitation laser. The atom can then emit another photon after a time, characterized by τ_R, and at that point the excitation emission cycle can start again. Since the spontaneos emission is a probabilistic process, the emission time is not the same for each cycle, which means that the stream of photons will not be exactly regular. However, it is clear that the probability for the emission of two photons with a time separation $<< \tau_R$ is very small. So we will have very few events where both the start and stop detectors of the HBT interferometer in figure 2.8 fire simultaneously, and so we shall have $g^{(2)}(0) \approx 0$.

We can ask a question why we do not observe the same antibunching effects from a conventional light source such as a discharge lamp. We can only observe antibunching effects if we look at the light from a single atom.

The photon-number correlation measurements for a coherent and for chaotic light of Gaussian frequency distribution are shown in figure 2.10. For a values of $\tau >> \tau_c$ the correlation time of the light, the correlation function factorizes and $g^{(2)}(\tau) \to 1$. The increased value of $g^{(2)}(\tau)$ for $\tau < \tau_c$ for chaotic light over coherent light $(g^{(2)}(0)_{chaotic} = 2g^{(2)}(0)_{coherent})$ is due to the increased intensity fluctuations in the chaotic light field. There is a high probability that the photon which triggers the counter occurs during the high intensity fluctuation and hence a high probability that a second photon will be detected arbitrarily soon. This effect known as photon bunching was first detected by Hanbury-Brown and Twiss.
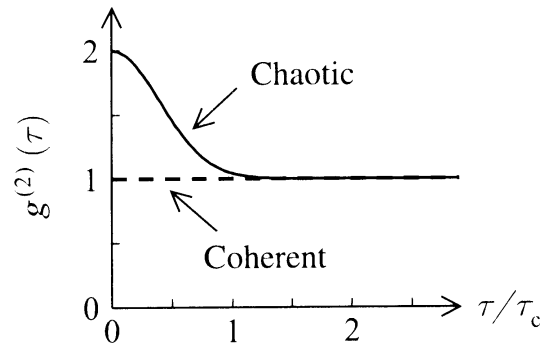
Figure 2.10: Correlations between pairs of photon counts for coherent and chaotic light.

Moreover, antibunching has also been observed from many other types of light emitters, including a number of solid-state sources, such as:

- Fluorescent dye molecules doped in a glass or crystal,

- Semiconductor quantum dots,

- Colour centers in diamond.

Chapter 3

Diamond

Semiconductor materials with band gaps ranging from the visible to the ultraviolet, referred to as wide band-gap semiconductors, have been extensively studied for potential applications in high-temperature electronics as well as for UV-visible emissive devices. Recent advances in the growth of diamond films at various temperatures and pressures have expanded the potential of diamond for use in optical and high-temperature electronic applications. An understanding of the optical and electronic properties of defects in diamond films is critical for the accurate evaluation of potential applications for diamond-based devices because of the significant effects of small point defect concentrations on the optical and electronic properties of these films.

In this chapter the most important material properties of diamond and aspects of growth and doping are briefly summarized. Diamond is transparent from wavelengths of 220 nm, and above in accordance with the 5.5 eV indirect bandgap.

3.1 Structure of diamond

The crystal structure of diamond is equivalent to a **F**ace **C**entered **C**ubic *(FCC)* lattice, with a basis of two identical carbon atoms: one at $(0, 0, 0)$ and the other at $\left(\frac{1}{4}, \frac{1}{4}, \frac{1}{4}\right)$, where the coordinates are given as fractions along the cube sides. This is the same as two interpenetrating FCC lattices, offset from one another along a body diagonal by one-quarter of its length. The conventional unit cell is cubic, with a side length a_0 approximately equal to 0.3567 nm at room temperature. From this we can derive a few other

quantities.

The C-C bond length d is equal to $\frac{1}{4}$ of the cubic body diagonal, so that $d = \sqrt{3}a_0 \approx 0.154$ nm. The conventional cell contains the equivalent of 8 whole C atoms. The atomic density is therefore $\frac{8}{a_0^3} \approx \frac{8}{(3.567\times10^{-10}m)^3} \approx 1.76 \times 10^{29} atoms/m^3$. Each atom can be thought of as a sphere with a radius of $\frac{1}{8}$ of the cubic body diagonal. The packing-fraction is therefore $8 \times \frac{4}{3} \times \pi \times \frac{(\sqrt{3}a_0/8)}{a_0^3}$, which simplifies to ≈ 0.34 [41].

3.2   Classification of Diamond

Diamonds can be mainly classified into four types, which are type *Ia*, *IIa*, *Ib*, and *IIb*. These types differ in their impurities therefore their optical ptoperties. Diamonds consist of carbon, and are extremely pure, but in almost all diamonds there are tiny proportions of other elements, interspersed within the carbon as part of their crystal structure. These *impurities* are not what are known but they are really single atoms or small clusters.

Type I

Type I diamonds contain nitrogen. Approximately 98% of all diamonds are this type. We can investigate type I diamond in two groups:

Type Ia

If the nitrogen atoms are clustered together within the carbon lattice, then the diamond is said to be a Type Ia-diamond. Ia diamond contains nitrogen up to 3000 ppm. Because these diamonds absorb blue light, they can have a pale yellow or brown color. 98% of natural diamonds are Type Ia.

Type Ib

Ib diamond contains up to 800ppm nitrogen. High Pressure High Temperature (HPHT) or Chemical Vapour Deposition (CVD) diamonds can be counted in this class. These diamonds absorb green light as well as blue light, and have a darker color than type Ia diamonds. Depending on the precise

Type	Prevalence	Feature
Ia	98%	clustered nitrogen atoms
Ib	0.1%	scattered nitrogen atoms
IIa	1-2%	highly pure carbon
IIb	0.1%	boron atoms

Table 3.1: Summary of Diamond Classification.

concentration and spread of the nitrogen atoms, these diamonds can appear deep yellow , orange, brown or greenish. Less than 0.1% of diamonds belong to Type Ib.

Type II

Type II are diamonds that contain no, or very few, nitrogen atoms.

Type IIa

These diamonds can be considered as the *purest of the pure* - they contain no, or negligible amounts of impurities (less then a few ppm nitrogen) and are usually colorless. Unless, that is, the carbon tetrahedrons that make up the diamond were twisted and bent out of shape while the diamond rose to the surface of the earth. An imperfect carbon lattice will make the diamond absorb some light, which will give it a yellow, brown or even pink or red color. 1-2% of diamonds belong to Type IIa.

Type IIb

These diamonds contain no nitrogen - but they do contain boron, which absorbs red, orange and yellow light. These diamonds therefore usually appear to be blue, although they can also be grey or nearly colorless. All naturally blue diamonds belong to Type IIb, which makes up 0.1% of all diamonds. It has a p-type conductivity, with an activation energy of 0.37 eV. The hole mobility measured at room temperature is 1500 cm^2/V sec.

High Pressure, High Temperature, HPHT

Under high temperature and high pressure conditions graphite transforms to dimaond and the graphite which is transformed to diamond does not convert back to graphite during the cooling period. Diamond synthesis is based on this idea.

There are two main press designs used to supply the pressure and temperature necessary to produce synthetic diamond. These basic designs are the belt press and the cubic press.

To use the belt press, wherein upper and lower anvils supply the pressure load and heating current to a cylindrical volume. This internal pressure is confined radially by a belt of pre-stressed steel bands. A variation of the belt press uses hydraulic pressure to confine the internal pressure, rather than steel belts.

The second type of press design is the cubic press. A cubic press has six anvils which provide pressure simultaneously onto all faces of a cube-shaped volume. A cubic press is typically smaller than a belt press and can achieve the pressure and temperature necessary to create synthetic diamond faster. However, cubic presses cannot be easily scaled up to larger volumes.

Experiments with synthetic and natural diamonds treated at high temperatures ($1700 - 2800°C$) and high pressures (6-8 GPa; HTHP) have shown that, with time, lattice defects can be altered or repaired.

3.3   Defects in Diamond

Defects in the crystal lattice of diamond are common; they may be the result of extrinsic substitutional impurities, or intrinsic (interstitial and structural) anomalies. All diamonds possess crystal lattice defects of some sort; the defects themselves may be either anthropogenic or natural, epigenetic or syngenetic. The material properties of diamond are affected by these defects and determine to which type a diamond is assigned; the most dramatic effects are on a diamond's color and semiconductivity, as explained by the band theory.

The defects can be detected by different types of spectroscopy, including **E**lectron-**S**pin-**R**esonance(ESR), photoluminescence in ultraviolet light, and absorption of infrared light. The resulting absorption spectrum can then be analyzed, identified, and used to separate natural from synthetic or enhanced diamonds.
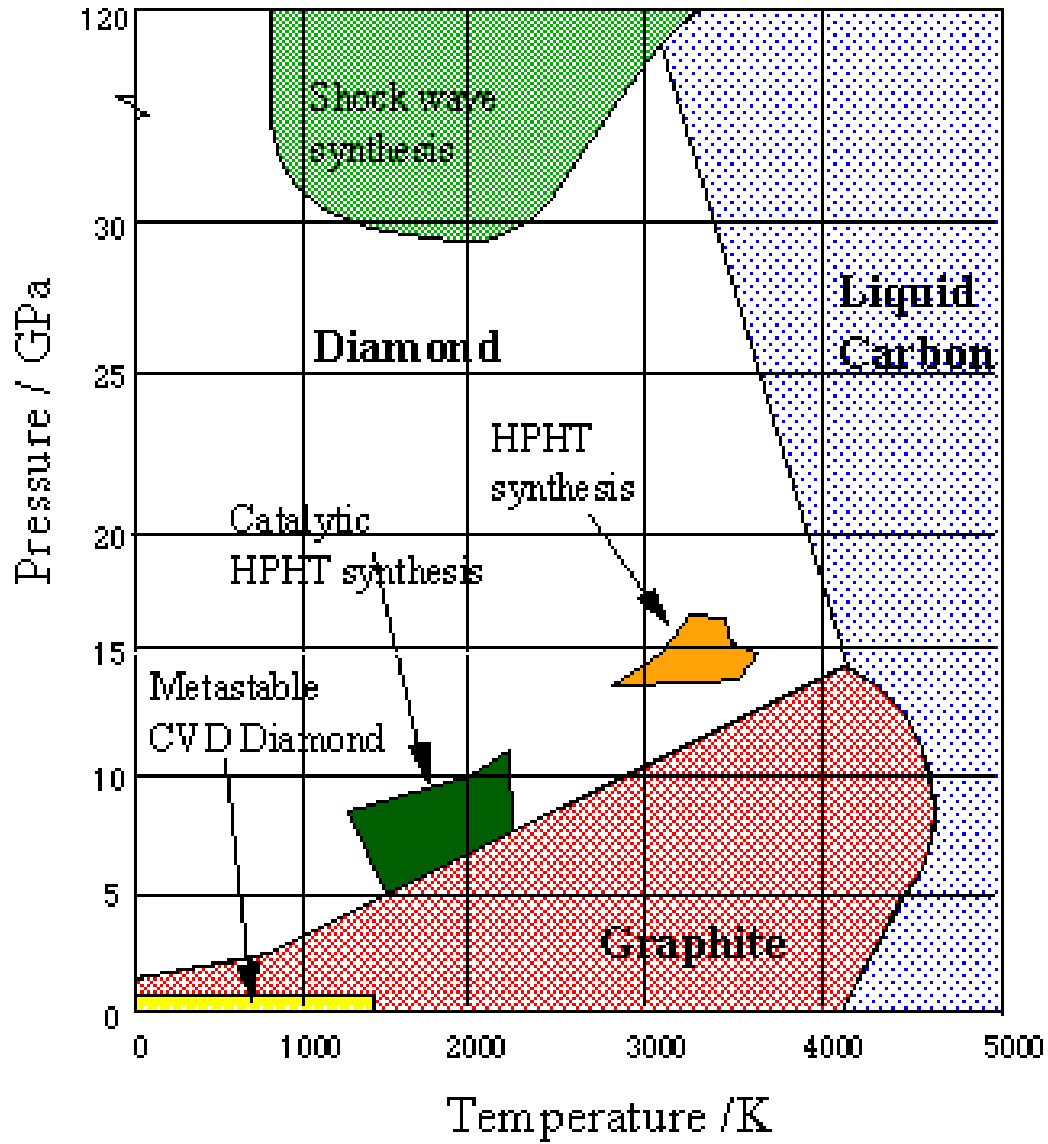
Figure 3.1: From: F.P. Bundy, Pressure vs. Temperature Phase and Reaction diagram for elemental Carbon, 1979; J. Geophys. Res. 85 (B12) (1980) 6930.

Since the energy of the ground and excited states of a colour center must lie inside the band gap, diamond offers a big playground for different colour centers because of it's large band gap. More than 500 colour centers are documented [42].

Vacancies

All diamond contain typical intrinsic or self-defects: vacancies, dislocations, and interstitial atoms. A vacancy is an empty position in a lattice. Vacancies may be affected or created by radiation damage high energy subatomic particles knock carbon atoms out of the lattice. The vacancies interact with interstitial atoms and act as color centers by absorbing visible light, thus producing green or blue colors in *Type I*, and brown colors in *Type IIa* diamond. Vacancies can be detected by ultraviolet fluorescence, as well as by a characteristic absorption line at 741.2 nm, termed the GR 1 (General Radiation) line. This line disappears if the diamond is annealed above $400°C$, after which a number of additional lines (e.g. 575, 595, 503 [H3 center], 497, 1935 [H1c center], and 2924 [H1b center] nm) are formed[1]. Defects in natural diamond are produced by color treatments. In our case, we have detected **Si**licon-**V**acancies(SiV) central wavelength at 738nm absorption line.

The annealing process also allows carbon atoms neighboring a vacancy to jump into a vacant place and leave an empty position in the diamond lattice; by this process a vacancy can migrate through the diamond, and can form compound defects with other vacancies, interstitial atoms (forming Frenkel pairs [41]), or nitrogenous defects (N-V centers). The newly-formed compound defects are optically active, the precise color dependent on the annealing time and type of pre-existing defects present. Vacancies can also be created or modified by HTHP treatment.

3.4   Colour centers

Fourier transform spectroscopy (FTIR) and Raman spectroscopy are used to analyze the visible and infrared absorption of suspect diamonds to detect characteristic absorption lines, such as those indicative of exposure to high temperatures.

---

[1] $http://www.gemlab.net/research1_4.htm$

Properties of Si-V centers

Si-V centers are not found in natural diamond. In 1981 a sharp line at the energy of 1.68 eV in the spectrum of silicon ion implanted diamond was observed by CL-spectroscopy (cathodoluminescence). The quadratic dependence of this CL-line intensity on the ion dose has lead to a hypothesis that a kind of Si_2 colour center is produced by the ion implantation [43]. But during ion implantation other kinds of defects are also produced amongst which neutral vacancy has a similar wavelength ZPL. This results in ambiguity. Only in 1995 the ZPL of this center has been resolved to 12 different lines at low temperatures which are grouped in 3 sub groups with each 4 lines [44]. The relative abundance of the 3 natural isotopes of Si in nature can be deduced from the different strengths of optical absorption of the 3 groups ($^{28}Si,^{29}Si,^{30}Si$). From this it can be proven that a 738 nm ZPL is generated from silicon atoms. The fact that, diamonds with Si impurities show these fluorescence lines only after that they are bombarded to electrons and heated to over $600°C$, hints towards vacancies taking part in these centers.

From the four different lines with in a subgroup of lines an energy scheme is proposed as given in in figure 3.2. However the real configuration of this center so far unclear. Polarized luminescence measurement have shown that the centers has a $\langle 110 \rangle$ symmetry axes [45]. Theoretical calculations predict a model with a single Si atom and a neighboring vacancy site [46].

Therefore it is energetically unfavorable for the Si atom to occupy the carbon atom lattice position and hence it lays at an interstitial lattice position. It follows that, in this configuration Si atom lays in the center of a kind of double vacancy position as shown in figure 3.2 schematically. This model is able to explain the doublet structure of the ground and the excited states and also delivers a theoretical value of the transition energy which lays close to the experimentally observed energy value. In addition the model predicts high stability and a 3 nanosecond lifetime of the excited state which is experimentally confirmed as well. CL- measurements at high temperatures has shown that the Si-V centers remain stable up to $1350°C$ [48]. The lifetime measurement of fluorescence of the center in CVD- diamond shows a lifetime of 1 to 4 ns at different temperatures and diamond qualities [49].

So that this model is taken to be true on ground for these findings and
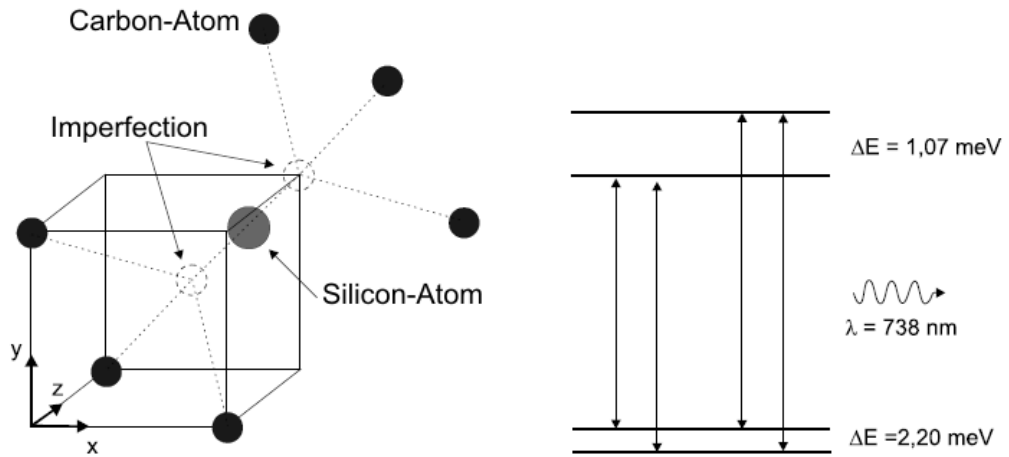
Figure 3.2: Theoretical model of energy scheme of SiV center [47].

will be used for description of Si-V centers in this work. For application as single photon source the fluorescence spectrum and the radiative transition rate are of interest. Since the splitting of the ground and excited states are very small these fine structures can not be observed at room temperature. In the theoretical configuration Si atom has no direct binding with the diamond lattice. Therefore the center couples only weakly to the diamond phonons. This results in a fluorescence spectrum at room temperature with a sharp ZPL with a width of 10 nm width and a very weak vibrionic side band. Opposingly, most of the other types of colour centers do have a wide band fluorescence spectrum. The 4ns lifetime of the excited state is also unusually short which enables high repetition rate in a single photon source. The known data of the other colour centers show longer lifetimes, for example, N-V centers have a lifetime of 13 ns. The relatively narrow fluorescence spectrum at room temperature and the short lifetime makes the Si-V center a very good candidate as a single photon source.

Raman-Scattering

Raman scattering is the inelastic scattering of a photon which creates or annihilates an optical phonon. When light is scattered from an atom or molecule, most photons are elastically scattered which is known as Rayleigh scattering. The scattered photons have the same energy and, therefore, the same wavelength as the incident photons. However, a small fraction of light ,approximately 1 in 10^7 photons, is scattered at optical frequencies different from, and usually lower than, the frequency of the incident photons. In a gas, Raman scattering can occur with a change in vibrational, rotational or electronic energy of a molecule. The Raman effect was first reported by C. V. Raman and K. S. Krishnan, and independently by Grigory Landsberg and Leonid Mandelstam in 1928.

The interaction of light with matter in a linear regime allows the absorption or simultaneous emission of light with an energy precisely matching the difference in energy levels of the interacting electrons. The Raman effect is a nonlinear (third order) effect.

The Raman effect corresponds, in perturbation theory, to the absorption and subsequent emission of a photon via an intermediate electron state, having a virtual energy level. When there is no energy exchange between the incident photons and the molecules no Raman effect occurs. Energy exchanges occur between the incident photons and the molecules. The energy differences are equal to the differences of the vibrational and rotational energy-levels of the molecule. In crystals only specific phonons are allowed (solutions of the wave equations which do not cancel themselves) by the periodic structure, so Raman scattering can only appear at certain frequencies. For amorphous materials like glasses, more phonons are allowed and thereby the discrete spectral lines become broad. If molecule absorbs energy Stokes scattering takes place. The resulting photon of lower energy generates a Stokes line on the red side of the incident spectrum. If molecule loses energy we can talk about anti-Stokes scattering where Incident photons are shifted to the blue side of the spectrum, thus generating an anti-Stokes line.

Raman Effect can take place for any frequency of the incident light. In contradistinction with the fluorescence effect, the Raman Effect is therefore not a resonant effect. The Raman spectrum in monocrystalline diamond consists of a first order peak at 1332.5 cm^{-1} and second-order (two-phonon) spectrum around 2500 cm^{-1}. Two broad bands at about 1550 and 1350 cm^{-1} are attributed to the amorphous sp^2 phase. A broad peak at 1100 cm^{-1} is ascribed to the amorphous sp^3 carbon phase. It can be excited exclusively
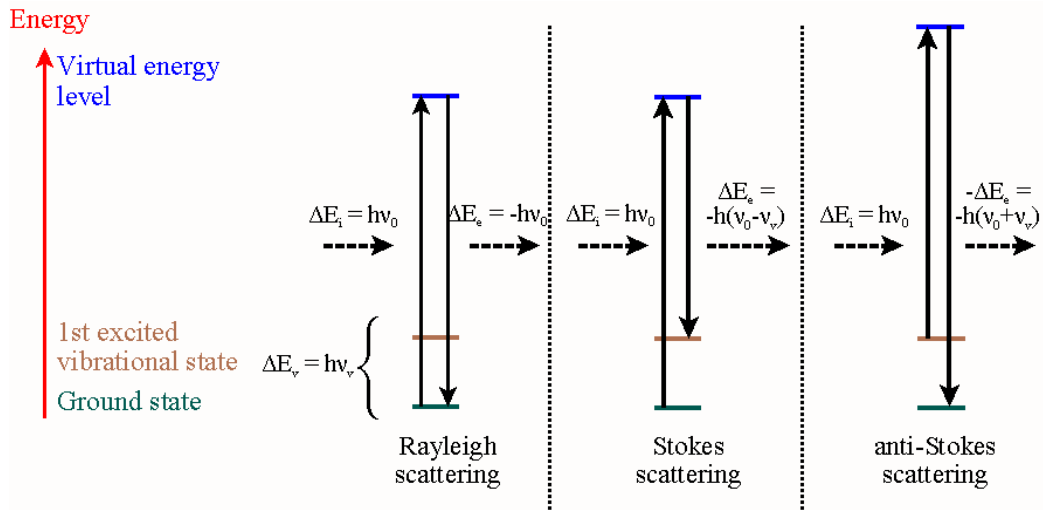
Figure 3.3: The different possibilities of visual light scattering: Rayleigh scattering (no Raman effect), Stokes scattering (molecule absorbs energy) and anti-Stokes scattering (molecule loses energy)

by UV light (> 4 eV) and is typically not observed in common Raman [50] (figure 3.4). Graphite shows a single peak at 1581 cm^{-1}.

The spectra are normally composed of a narrow ZPL (zero phonon line) and vibronic sidebands .The ZPL stems from a direct electronic transition whose line width originates from only local strain of the lattice. If an absorption or an emission does simultaneously excite a phonon in a lattice vibrational mode the signals of absorption or emission will be detected at shorter or longer wavelengths. The name vibronic means a phonon-electron transition. The structure of the sidebands is unique for each colour center so that they can be used in identification of colour centers.
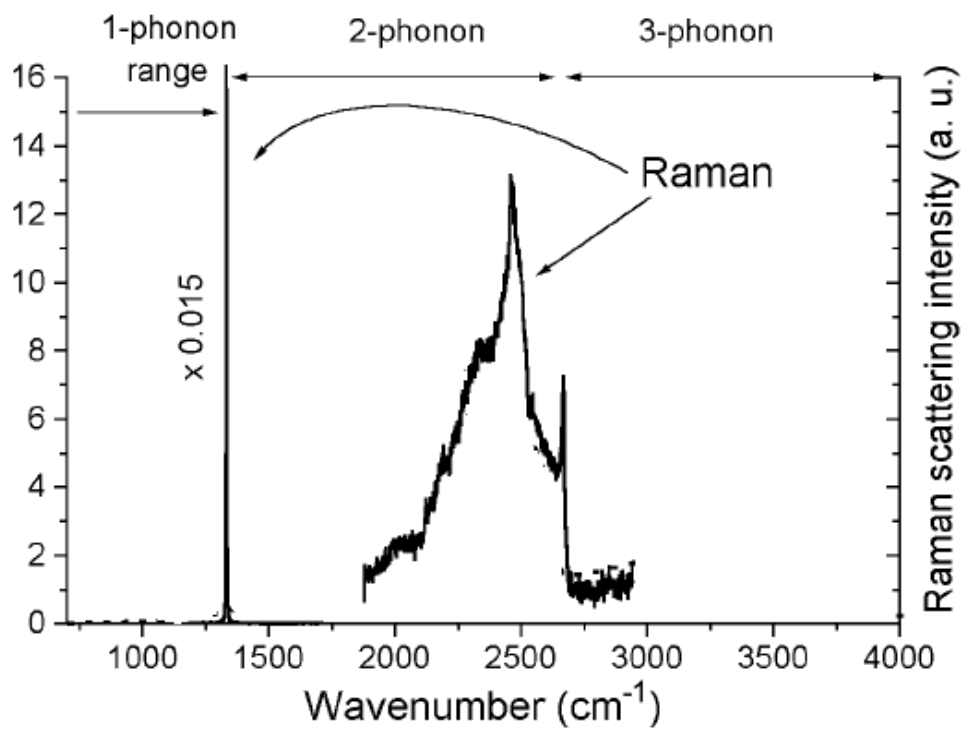
Figure 3.4: Room-temperature Raman spectra from IIa diamond

Chapter 4

Experimental Setup

4.1 Introduction

In this section, the preparation of samples and the optical setup will be described. The color centers in diamond are detected by a confocal microscope. The fluorescence which comes from the center is sent to a home-made spectrometer via a fiber coupler to measure the spectrum or it is sent to a HBT setup to measure the anti-bunching property of light.
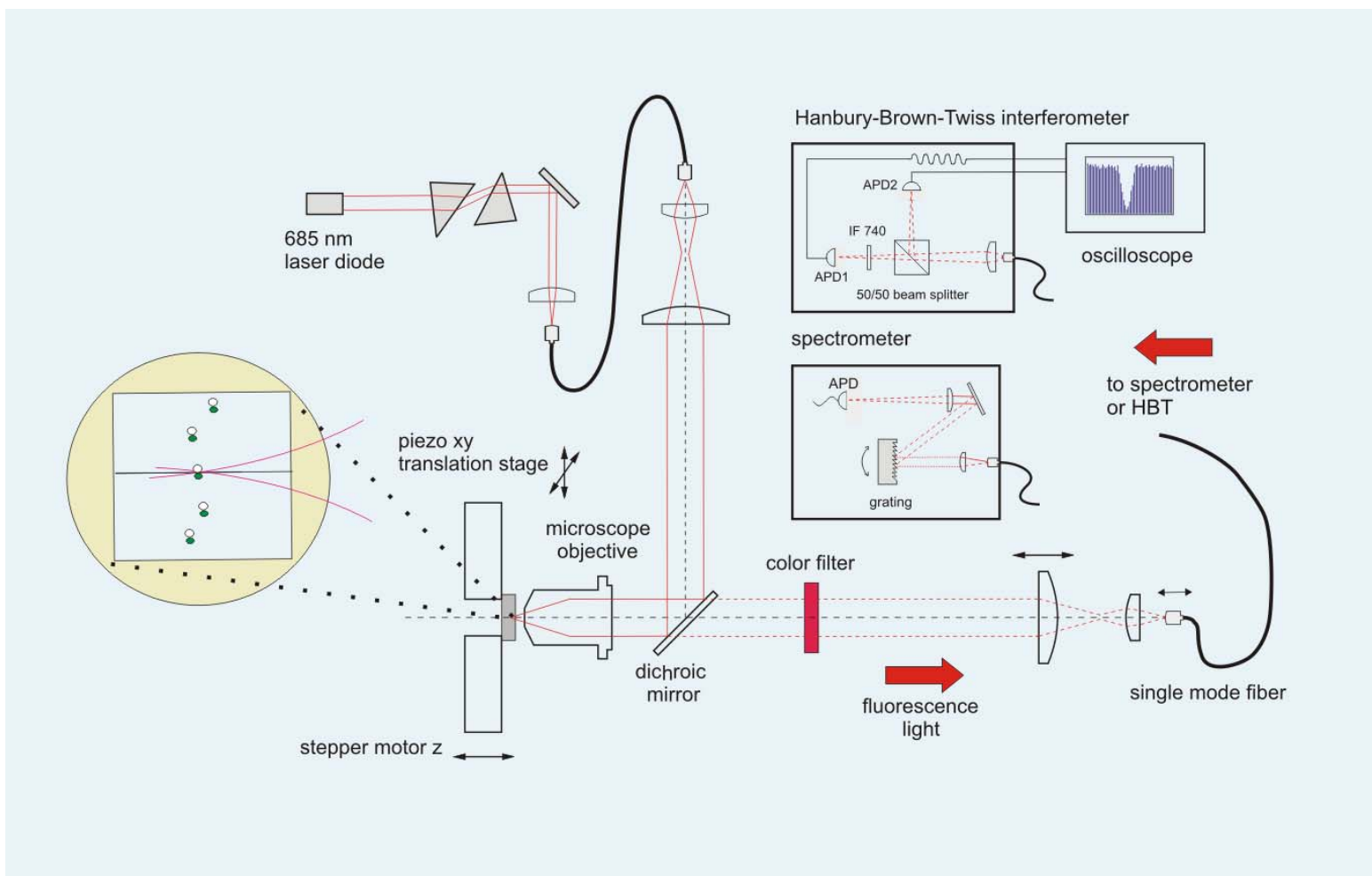
Figure 4.1: Schematic diagram of the SetUp.

4.2   Sample Preparation

We bought the *IIa* diamond samples, which are colour free, from Druker International[1]. These diamonds are synthetic grown diamonds and cut by a laser into cubes with $0.5mm$ side length. Two parallel surfaces are polished to form windows where the laser light can go through the sample.

Colour centers in the diamonds samples are produced by ion implantation at the Tandem Laboratories at Bochum University[2]. First, silicon is ionized and afterwards the ions are accelerated under 4MeV and implanted to the samples. Some of the samples are processed in inert gas atmosphere under $1300°C$. Multiply ionized ions are used, thus high energies have been reached. The SiV centers are $2\mu m$ below the surface where they form as monolayer. After ion implantation the sample is heated, in a vacuum chamber. There is a ceramic inside the chamber which is surrounded by a tantal coil, with 0.5mm thicknesses. A current is applied to the coil to reach $1000°C$. The coils are isolated by a PVC inlet from the wall of the chamber. By third inlet the temperature measurement can be done with a thermo couple, which is inserted into the ceramic cylinder. The current can be applied maximum 8mA. The role of the ceramic cylinder is to isolate the tantal coil from thermo couple to block the electrical conduction.

Two Aluminum foils, which avoid the heat-dissipation, surround the tantal coil. The inside walls of the vacuum chamber is also covered with an Aluminum foil to reflect the heat radiation back. The pressure in the vacuum chamber can be measured by pressure gauge. The inside pressure is kept under 10^{-2} mbar.

In the heating process up to $1300°C$, some of the implanted silicon ions can combine with a vacancy to a SiV center. The graphite which growth on the sample surface, is removed by a solution which includes $K_2Gr_2O_7$ solved in 70% H_2SO_4. We put the diamond samples into this solution and heat it up to $180°C$ for 2 minutes.

---

[1]http://www.fbg.nl/
[2]III. Experimental physics Institute Micro Beam Group

4.3 Optical Setup

4.3.1 Confocal Microscope

A confocal microscope creates sharp images of a specimen that would otherwise appear blurred when viewed with a conventional microscope. This clear image is achieved by excluding most of the light from the specimen that is not from the microscope's focal plane. The image has less haze and better contrast than that of a conventional microscope.

Martin Minsky is the scientist who invented the first Confocal microscope in 1955. It performs a point-by-point image construction by focusing a point of light sequentially across a specimen and then collecting some of the returning rays. By illuminating a single point at a time he avoided most of the unwanted scattered light that obscures an image when the entire specimen is illuminated at the same time. Additionally, the light returning from the specimen would pass through a second pinhole aperture that would reject rays that were not directly from the focal point. The remaining *desirable* light rays would then be collected by a photomultiplier and the image gradually reconstructed using a long persistence screen. Minsky scanned the specimen by moving the stage rather than the light rays to build the image .This was to avoid the challenge of trying to maintain sensitive alignment of moving optics. He used a 60 Hz solenoid to move the platform vertically and a lower-frequency solenoid to move it horizontally, Minsky managed to obtain a frame rate of approximately one image every 10 sec.

The modern confocal microscopes still uses the same techniques as Minsyk did like the pinhole aperatures and point-by-point illumination of the specimen. With the growing technology improvements in speed and image quality is reached.

In our set up, a free running laser diode which produces 50 mW optical power at a wavelength of 685nm is used to excite the SiV centers in the sample. The laser light is coupled into a single mode fiber to achieve a Gaussian TEM_{00} mode. Before coupling the laser into a fiber two amorphic prism pairs[3] are used to shape the laser profile.

After the fiber two lenses are used to adjust the beam diameter to the microscope objective. A filter supresses unwanted wavelengths emitted by the laser diode. A dichroic mirror reflects the excitation light. The excitation

---

[3]For detailed information see http://www.thorlabs.com/

light continues the path to the objective and is focused on the sample. The NA of the microscope objective is 0.85. With this objective we can get a spot size of 250nm. The sample is mounted on a piezostage to move it in the x, y plane and the piezostage can be moved in z direction with the help of a stepper motor. The excitation of the colour centers and collection of the flourescence light is done by the same objective. The fluorescence light is collected by the same objective and seperated from the excitation light by the dicroic mirror. It is coupled into single mode fiber and guided to detectors. This single mode fiber is used for special filtering instead of a pinhole which can be seen in standard confocal microscopes. The single mode fiber guides the flourescence light to a HBT setup or spectrometer.

The overall resolution of the microscope in x, y is $0.5\mu m$ and in z direction $2.5\mu m$ which is enough to detect single colour centers in diamond. We have used a diamond Solid Immersion Lens (SIL) to get a smaller spot size to have a better resolution. In conclusion, the collection efficiency can be improved by SIL.

4.4   Solid Immersion Lens-SIL

A solid immersion lens is a powerful device to study the optical properties of microstructures due to its high spatial resolution beyond diffraction limit [51], as well as high efficiency of light collection [52]. The enhancement in the resolution is obtained by forming a diffraction limited focused light spot directly at the flat SIL-Sample interface. This way the size of spot scales like $\frac{\lambda}{n}$. There are two configurations of solid immersion lens, one is hemispherical-SIL(h-SIL) which improves the spatial resolution by a factor of n, where n is the refractive index of the material. This SIL is universal for any wavelength. The other one is super-spherical-SIL (s-SIL) in Weierstrass optics that further improves spatial resolution and collection angle by another factor n [53], but is designed only for one wavelength. We have used a *IIIa* diamond h-SIL in our experiment which has a $0.45mm$ radius to improve the collection efficiency by increasing the solid angle.
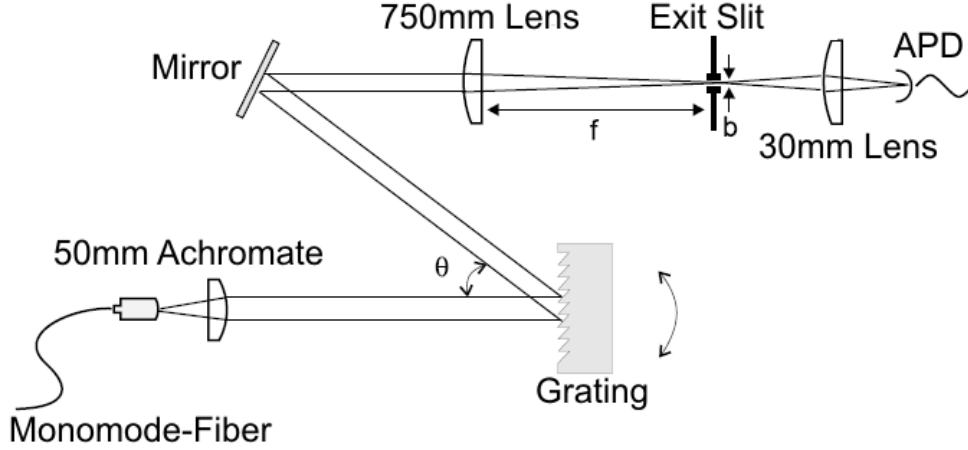
Figure 4.2: Schematic diagram of the home-made spectrometer.

4.5 Spectrometer

Colour centers can be identified by their spectra. The fluorescence collected by the microscope is analyzed with a home made spectrometer. Based on the measured spectrum we can find out if the fluorescence comes from a color center or not. The spectral resolution limit of a grating spectrometer is given by:

$$\Delta\lambda = \frac{\lambda}{mN} \quad , \tag{4.1}$$

where m is the diffraction order and N is the period number $\left(\frac{rule}{mm}\right)$. Assume that we have a detector which has width b behind a lens with focal length f. The wavelength that the detector will detect depend on $\frac{b}{f}$.

$$\Delta\lambda = \frac{d\cos(\theta)\Delta\theta}{m} = \frac{bd\cos(\theta)}{mf} \quad . \tag{4.2}$$

We are using a 1800 $\frac{rule}{cm}$ grating. Our light illuminates a 2500 rule-area. We can get 0.3 nm spectral resolution overall at 700 nm wavelength. This grating is used in first order. The light collected is focused with a lens which has a 750 mm focal length and passed through an exit slit. We use a lens which has 30 mm focal length to focus the light to an APD.
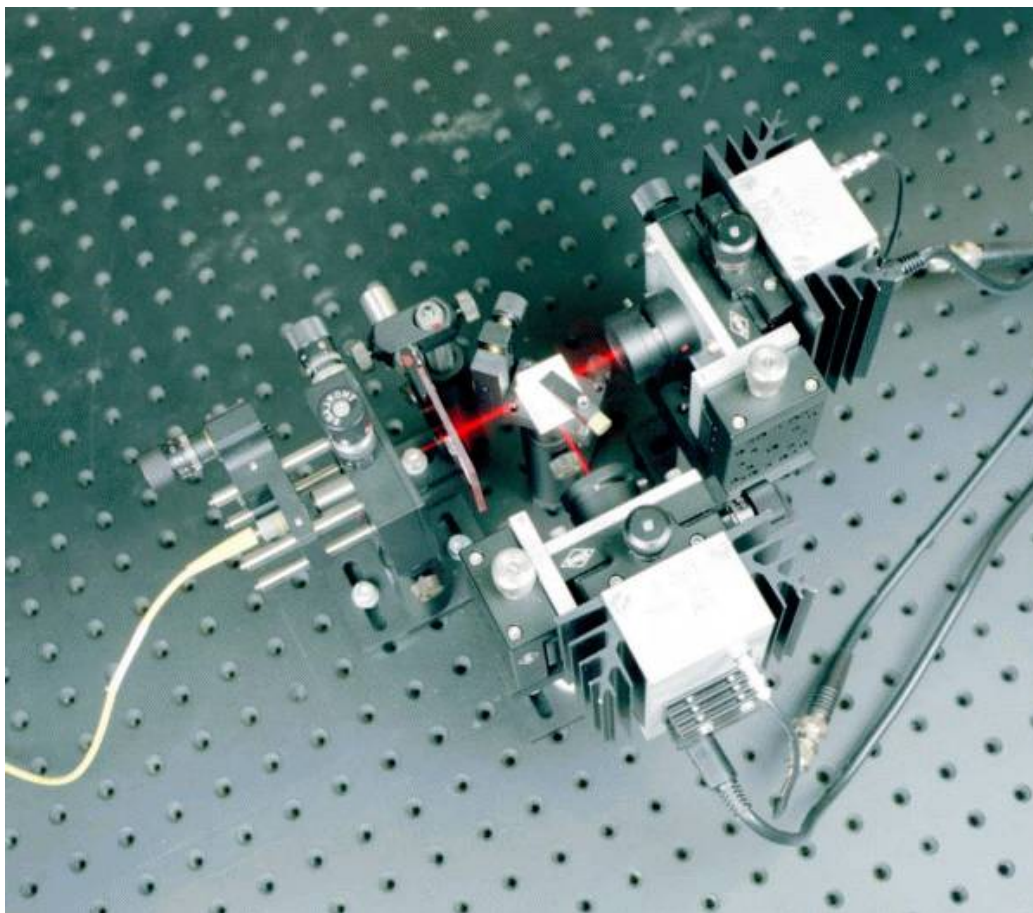
Figure 4.3: Hanbury-Brown-Twiss configuration for measuring the photon statistics.

4.6 Hanbury-Brown and Twiss Setup-HBT

To ensure that we really detect flourescence from a single colour centers (and therefore can conclude that we have a single photon source) we measure the autocorrelation function.

In HBT setup two single photon detectors are placed behind a 50:50 beam splitter. One of the detectors is the "STOP" and the other is the "START" detector. The time difference between two signals is measured electronically and the histogram of the time differences is made. The START signal is passed through a 60 ns delay path. $g^{(2)}(\tau)$ function can be measured for negative time difference. For cw excitation equation (2.14), $g^{(2)}(\tau)$ for

$\tau \gg \tau_c$ takes the value 1. In our measurement τ_c is only some nanoseconds, so we do not want to measure values bigger than $120ns$. To do this an artificial STOP signal is made. The measurement efficiency can be improved in this way, because of the low count rate.

Because the APD also fluoresce an interference filter is put in front of the detectors to get rid of the optical cross talk. The interference filter is also used to select only defined wavelengths. The single photon detectors that we use are silicon APDs with an detection efficiency for single photons of 50%. In these diodes the incoming single photon causes an electron avalanche. During this avalanche and the following slove build up of the over bias voltage the detectors do not response to other photons. This time is called dead-time. High intensities of bigger than 10^6 counts/sec cause saturation on APD.

Chapter 5

Experimental Results

5.1 Introduction

The SiliconVacancy (SiV) defect center in diamond has been observed and studied in detail spectroscopically as an individual quantum object using single molecule spectroscopy (SMS) [54]. Therefore, single SiV centers can be used as single photon sources exciting individual SiV centers and counting emitted fluorescence photons with an appropriate photon detector. One can measure the average fluorescence intensity and the second order fluorescence intensity correlation function; this work is mainly about to study the enhancement of fluorescence collection efficiency from Single Silicon Vacancy centers by putting a diamond Solid Immersion Lens (SIL) onto IIa diamond samples. By using SIL, we showed that the single photon count rates can be improved by a factor of eight in the case of good contact with SIL and sample surface. In a confocal microscope setup individual SiV centers are excited and the fluorescence photons are counted with an appropriate single photon detector.

This chapter presents the results of the experiments and compares the results to the theory developed in Chapter 2 and 3. Three-level system which is used to explain energy levels will be metioned. The data in this chapter present a novel way of observing a single photon within a diamond.

5.2   3-level system

To investigate dynamical processes of photoluminescence, we can model the single color center response within the framework of a three-level system.[1] A schematic level representation of the colour centers is shown in figure 5.1, with the three main electronic states involved in absorption, fluorescence, and intersystem crossing.

The ground state of the SiV center is a singlet state. The first excited singlet state is the one reached after absorption of a photon. But there is another excited state at lower energy (because of exchange interaction) than the first excited singlet which is the triplet state T. Transitions between singlet and triplet states are called Inter System Crossing (ISC).
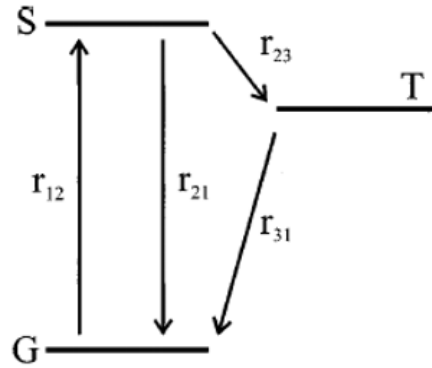
Figure 5.1: Schematic energy scheme *Jablonski Diagram* showing the ground (G), excited singlet (S), and triplet (T) states, and the various transition rates between the states [56].

However, the triplet state plays a central role in the photodynamics of the colour center. The emission of light occurs via transitions between the singlet excited state and the ground state. There is also a triplet state that the

---

[1]The evolution of the system can be described by optical Bloch equations for a three-level system. In general, such a system can only be solved numerically [55]. However, due to the high dephasing of the optical transition at room temperature (≈ 400 GHz), the optical Bloch equations can be reduced to rate equations and solved analytically.

system enters and leaves nonradiatively. In the emission spectrum, the bright intervals(fluorescence) correspond to the evolution of the system between the ground and excited singlet states. If the system undergoes a transition to the metastable state, it will not fluoresce and a dark interval will occur with a length equal to the lifetime of the metastable state.

These dynamics can be described by the following set of rate equations for populations p_1, p_2, p_3 of the three levels

$$
\frac{d}{dt}\begin{pmatrix} p_1 \\ p_2 \\ p_3 \end{pmatrix} = -\begin{pmatrix} r_{12} & -r_{21} & -r_{31} \\ -r_{12} & r_{23}+r_{21} & 0 \\ 0 & -r_{23} & r_{31} \end{pmatrix}\begin{pmatrix} p_1 \\ p_2 \\ p_3 \end{pmatrix} \tag{5.1}
$$

where r_{nm} (with n,m = 1,2, 3) denotes the transition rate from level (n) to level (m). We can assume that transition rates r_{23} and r_{31} to and from the metastable level, respectively, are small compared to the rate of decay r_{21} from excited to ground level.

In order to determine the maximum emission rate and to derive the fluorescence quantum efficiency, the fluorescence saturation curve had been recorded which is shown in figure 5.2. In the low laser power regime, the fluorescence intensity is linearly increasing with laser power. For high laser powers, the influence of the metastable level increases, and the fluorescence intensity saturates. The saturation data have been fitted using

$$
F(P) = F_0 \frac{P}{P_{sat}+P} + \alpha P \quad , \tag{5.2}
$$

which can be derived for an ideal two-level systems [54] and the corresponding laser power for saturation is defined and F_0 is the fluorescence intensity corresponding to infinite laser power. αP comes from the backround fluorescence.

5.3   Spectrum of a single SiV center

There are more than 100 luminescent defects in diamond [57]. Many of them have been characterized by optical spectroscopy. The Silicon Vacancy colour centre has been studied which is among them. The bright fluorescence emitted by the defect with a zero phonon of line (ZPL) at 738 nm is due to
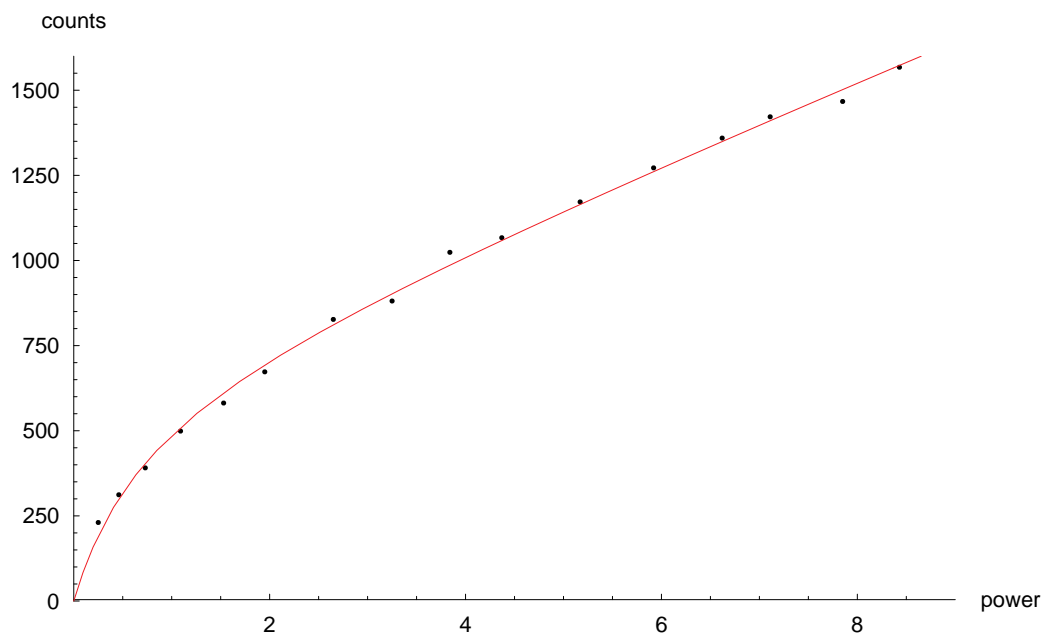
Figure 5.2: The fluorescence intensity saturation curve; symbols represent the experimental data and the red line a fit to data, according to equation (5.2) in the text.
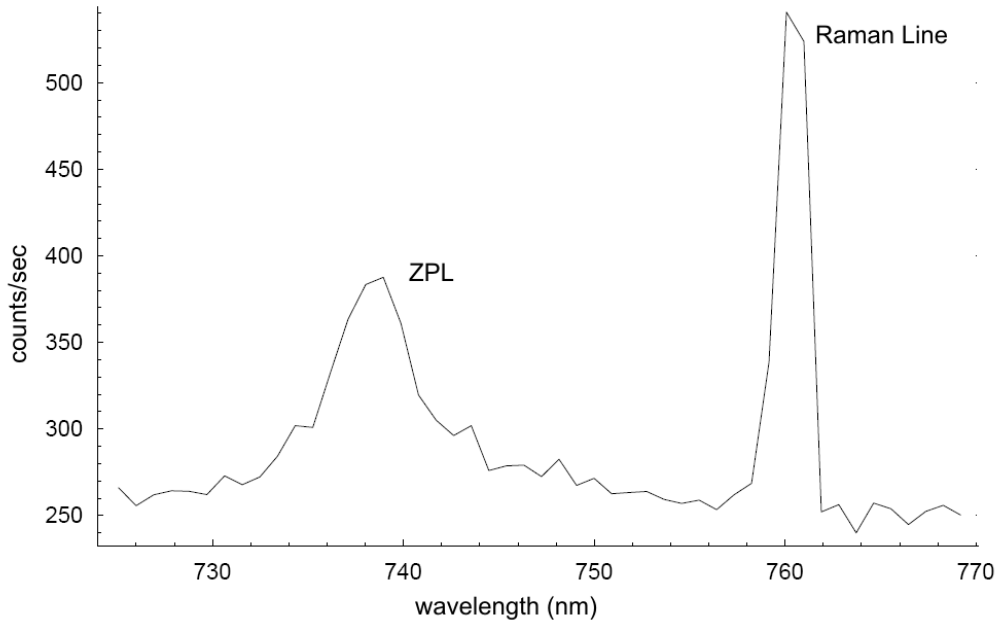
Figure 5.3: The narrow peak at 738 nm is the ZPL of the SiV centre The Raman scattering peak is at 760 nm.

an optical transition. The fluorescence emission spectrum obtained from a single defect centre is shown in figure 5.3.

The spectrum shows one pronounced zero-phonon line with only very weak vibronic sidebands at room temperature, and a very short photoluminescence lifetime of $1 - 4$ ns [46].

5.4   Finding single centers

To find single SiV centers in a sample, we first raster scan the sample $20\mu m \times 20\mu m$ without SIL to investigate the positions of the centers. Afterwards we did $2\mu m \times 2\mu m$ scans with type IIa diamond sample without Solid Immersion Lens in figure 5.4 to identify well-isolated photoluminescent emitters using a 685nm diode laser for continious wave (cw) excitation. A maximal optical power of 50 mW is focused on the sample by a high Numerical Aperture

($NA = 0.85$) microscope objective. The sample is mounted on a piezostage to move it in the x, y plane and the piezostage can be moved in z direction with the help of a stepper motor. The fluorescence is measured behind an interference filter with a central transmission wavelength at 740 nm and a bandwidth of 10 nm. The bright spot corresponding to SiV center appear clearly on the scan. All the centers that are measured without lens show the same properties.

Figure 5.5 shows a scan of the sample with SIL. The bright spots corresponding to SiV center appear clearly on the scan with higher count rate however we did not see this effect in all SiV centers. They show different brightness.

Figures 5.6 and 5.7 show the luminescence intensity profile in transversal direction for the emitter in figures 5.4 and 5.5, respectively.

5.5   Analysis of Fluorescence of Single Defect

Intensity autocorrelation measurements of the fluorescence light have been performed to demonstrate the sub-poissonian statistics of the light emitted by the centre. Using a start-stop scheme the coincidence rate between the two detectors of a Hanbury-Brown and Twiss interferometer has been measured. Obtained the data are equivalent to the second order intensity autocorrelation function for short time scales. The normalized autocorrelation function was obtained from a photon coincidence rate histogram [33]. Antibunching evidence of single center emission appears as a dip in the recorded delay function around $\tau = 60$ ns (electronic delay of 60 ns).

Data for a SiV center with SIL are presented in figure 5.10.[2] The correlation function plot for single SiV center in this figure provides plausible evidence of single photon, since the correlation function intensity drops to background for 60 ns time delay between detection at the two APDs. The remaining difference from zero at zero delay time results from the background, mostly related to the Raman scattering from the diamond lattice. In addition to antibunching, the autocorrelation function also shows photon bunching.

It is clear to see from the figure 5.10 that $g^{(2)}(\tau)$ reaches values greater than unity. This effect is due to the presence of a third state in which

---

[2]Due to the low count rate of SiV centers without SIL the autocorrelation measurements could not be observed.
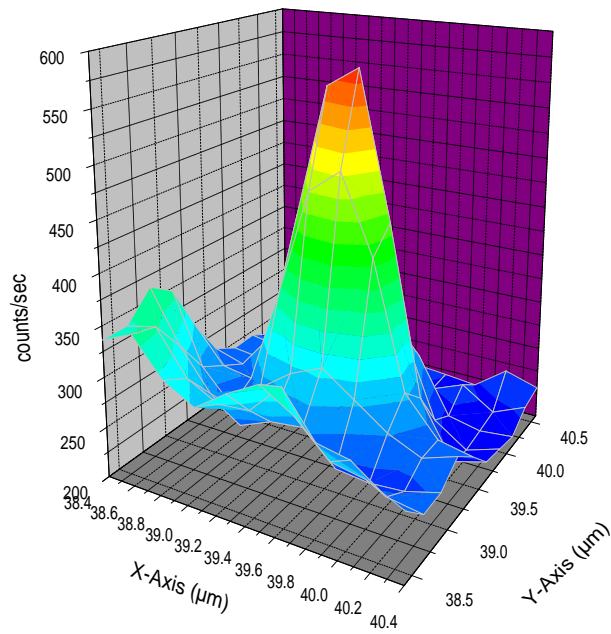
Figure 5.4: Fluorescence intensity raster scan $(2\mu m \times 2\mu m)$ of a IIa diamond sample performed about $2\mu m$ below the diamond surface showing luminescence from an isolated color center. The size of a pixel is 100 nm. The integration time per pixel is 1000 ms. One APD output in the HBT setup gives maximum counting rate 600 counts/sec.
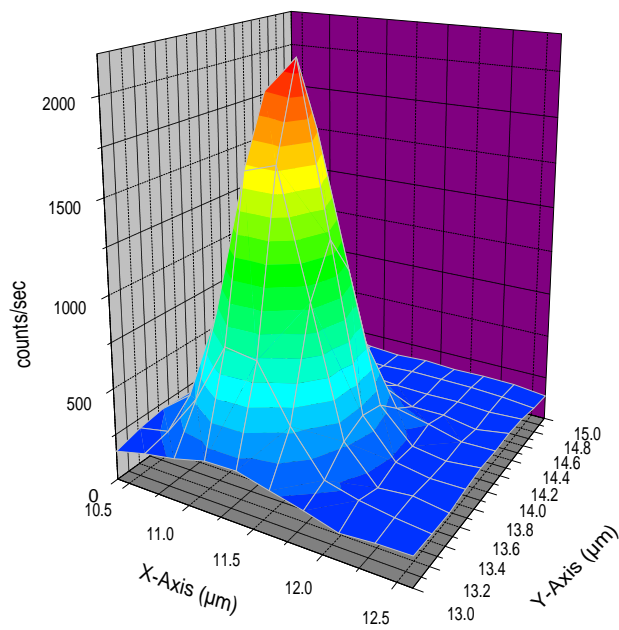
Figure 5.5: This fluorescence scan $(2\mu m \times 2\mu m)$ of a IIa diamond sample performed with the same parameters as in figure 5.4 with SIL and we observed high intensity compared to figure by a factor of 6.
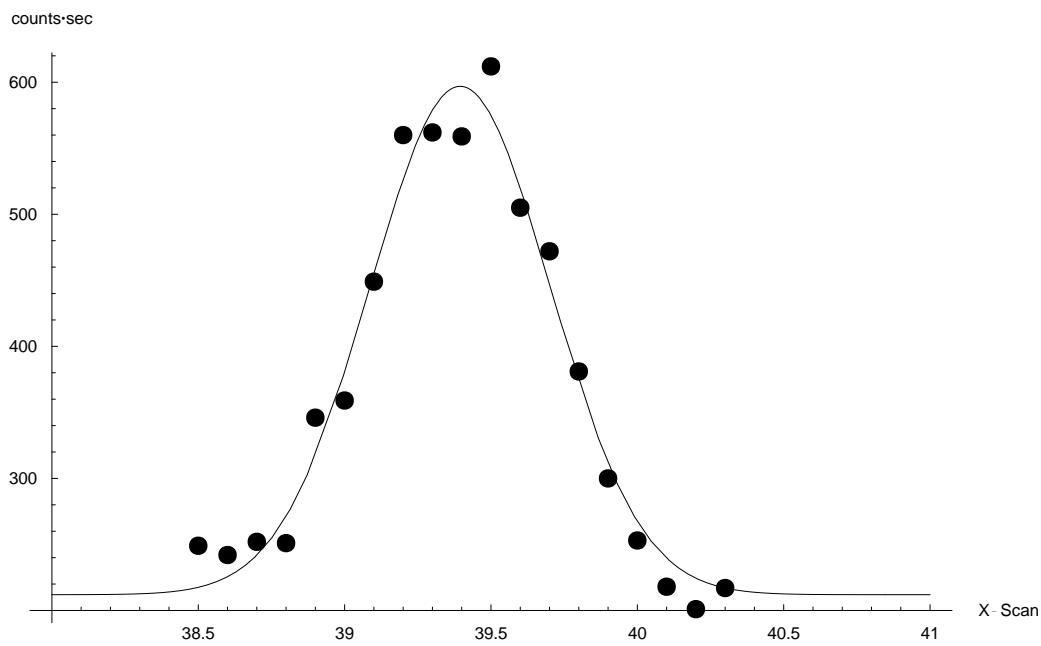
Figure 5.6: Line scan without SIL for figure 5.4 with $0.6\mu m$ FWHM. The data is shown together with a gaussian fit, which is used to evaluate the signal and background levels. The line scan in figure shows that the signal (S) to background (B) ratio is $S/B = 4$.
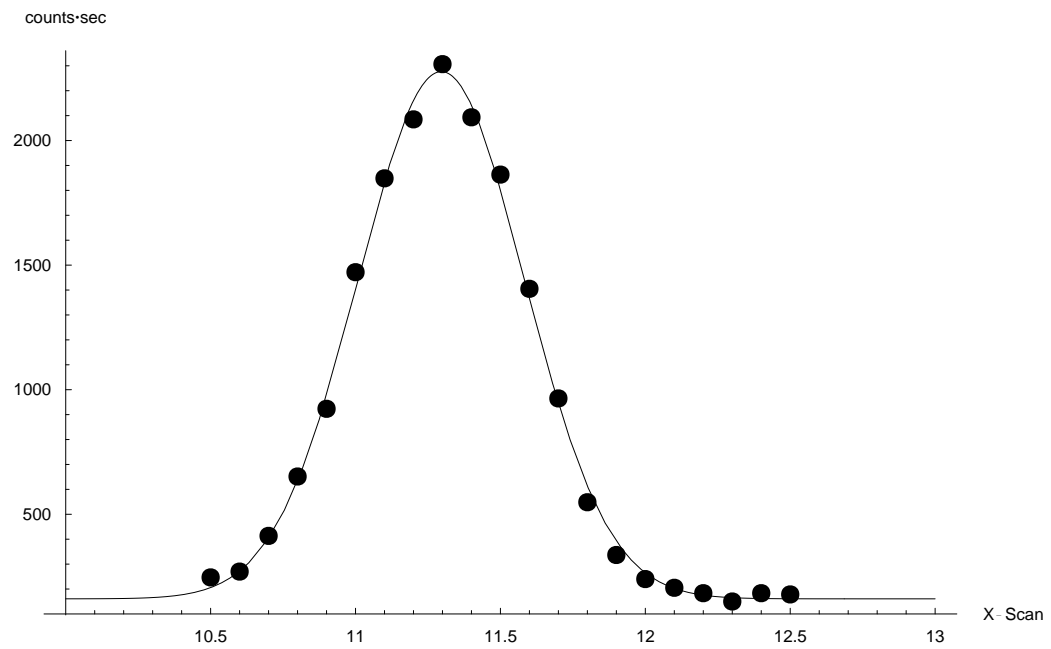
Figure 5.7: Line scan with SIL for figure 5.5 with $0.5\mu m$ FWHM. It can be seen that the spot size becomes smaller compared to the case without SIL which explains the better resolution. The data is shown together with a gaussian fit, which is used to evaluate the signal and background levels. The signal (S) to background (B) ratio is $S/B = 15.3$ which is improved by using SIL.
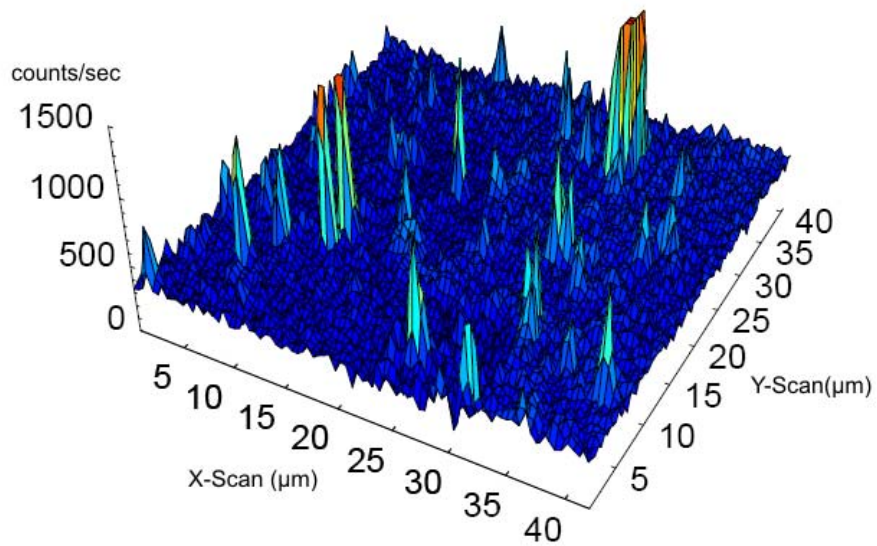
Figure 5.8: Scheme of the experimental measurements with images of single colour centers with SIL. Confocal fluorescence image ($40\mu m \times 40\mu m$) of SIV centers embedded in diamond with continuous-wave excitation at 685 nm.
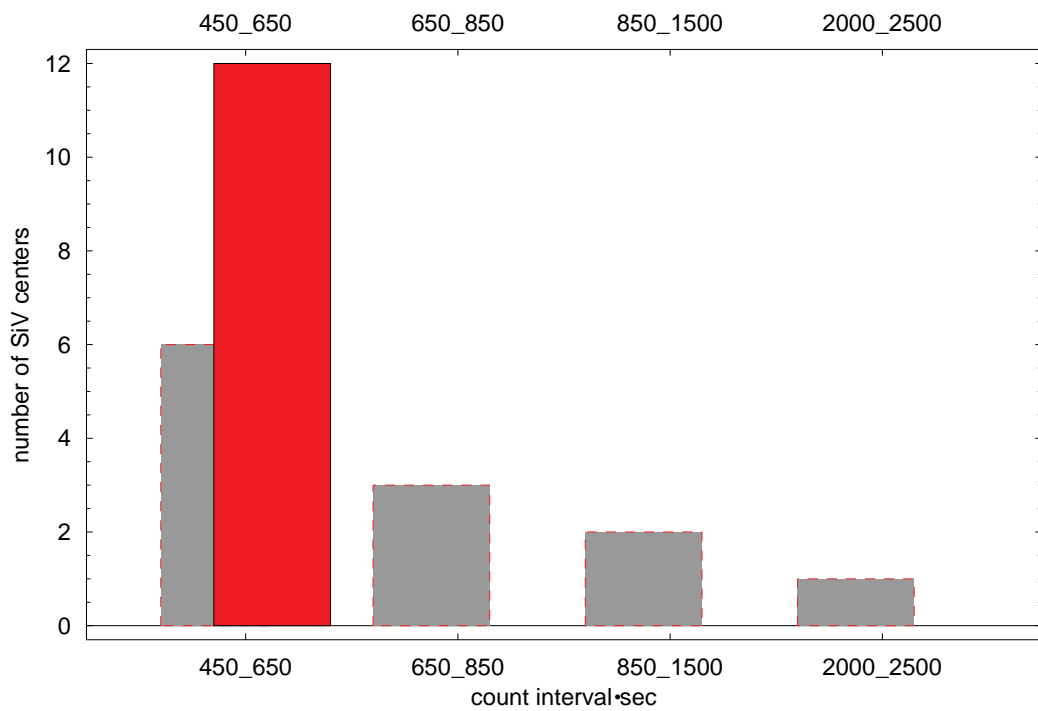
Figure 5.9: The histogram peak intensities for the SiV centers with and without SIL in $40\mu m \times 40\mu m$ region of diamond sample. The number of SiV centers without SIL are indicated by the red bar. All the centers show the same count rate. The number of SiV centers with SIL are indicated by the gray bars. The SiV centers show different count rates with SIL.
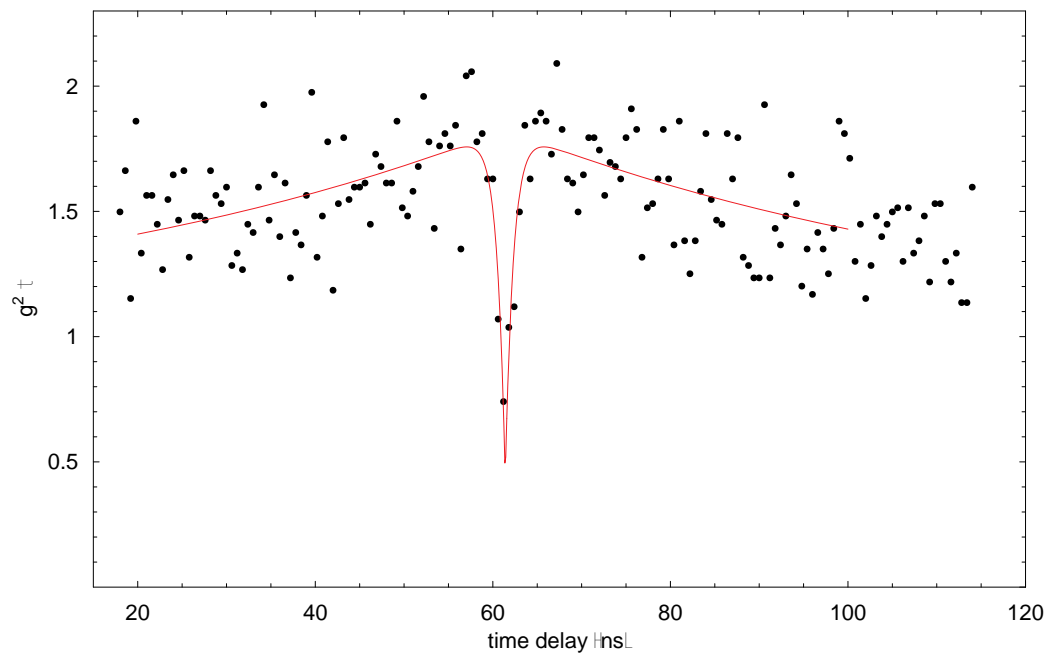
Figure 5.10: The fluorescence intensity autocorrelation function; the experimental data are shown in circle-shaped symbols, while the red line is the theoretical curve, calculated according to the procedure described in the text. The autocorrelation function shows a good contrast and presents a pronounced dip close to $\tau = 60ns$. Photon antibunching correlation measurements are carried out using the setup shown in figure 4.1.

the system can be shelved [58]. Blinking is a common phenomenon of the single-photon nature of the source. Several mechanisms are suggested to explain the blinking behavior: for instance, shelving (triplet blinking) to the long-living state, and fluctuations in the photo-physical parameters of the molecule and its local environment. Fluorescence has been observed in the saturation regime for hours without any photobleaching.

5.6 Experimental Difficulties

After the experiment was completely built and aligned precisely, we still had difficulties consistently measuring the signal. The main problem that we dealt with is the air gap between the sample and the SIL.

Aberrations and Allowances of hemisphere SILs

Solid immersion lens (SIL) have been used in various application in recent years. The basic principle of SIL is the same as that of oil-immersion microscopy and hence is well known. All solid state oil-free operation enables such advantages as no contamination of specimen and is very useful in vacuum and at low temperatures. A diamond SIL is used because it has the same refractive index as our diamond samples.

Cleaning operations are performed before all measurements. In our processes we performed 3-solvent cleaning, in which the solvents are distilled water, acetone (CH_3COCH_3), and isopropanol (p.a.) (($CH_3)_2CHOH$). The solvents are extremely pure and filtered in submicrons. Organic solvents are effective in removing oils, greases, waxes and organic materials. After each cleaning step samples are dried up by the nitrogen. After cleaning steps the SIL is put onto the sample in a clean room.

When one prepares and uses a SIL in practice, deviation from the ideal design degrades microscopic images. Thus, it is important to know aberrations of an imperfect SIL and its allowances. On the basis of point-spread function, three point should be considered [53]. There are aspheric error, a thickness error, and air gap. They are shown in figure 5.11 for PL microscopy without the para-axial approximation while using SIL.

In a perfect hemisphere SIL, there is no aberration for light focused into the sphere center, since all light rays incident normally to the hemisphere surface converge at the center.
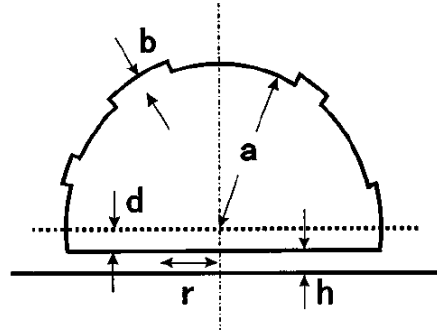
Figure 5.11: The schematic [59] of the typical errors in a hemisphere SIL: aspheric error **b**, a thickness error **d**, and an air gap **h**.

Since a hemisphere SIL is typically fabricated by grinding a ball lens with refractive index n and radius **a** into hemisphere, the first possible error is the deviation of the lens shape from the perfect sphere. From the quarter wavelength condition, the allowances for the aspheric error **b** is given by;

$$b < \frac{\lambda}{4(n-1)} \quad , \tag{5.3}$$

where λ is the wavelength of light in vacuum and n is the refractive index of SIL. The allowed **b** is smaller for larger n or for smaller λ. In our case, the wavelength is 689nm, n is 2.4 so by inserting these values into equation (5.3), we get $b < 114$nm. According to the information by the company, element6, **b** is smaller then 100nm. We thus do not have to care about the aspheric error **b**.

The second possible error is the thickness error of a SIL, where the excess thickness **d** from the radius, **a**, for hemisphere introduces the spherical aberration at the bottom surface in the SIL. The allowances for the thickness error **d** as,

$$|d| < \sqrt{\frac{2a\lambda}{n(n-1)}} \quad , \tag{5.4}$$

where **a** is 0.9mm in equation (5.4). In this case we get $d < 12.8\mu m$. According to the specification **d** is smaller than $1\mu m$ and thus also below the
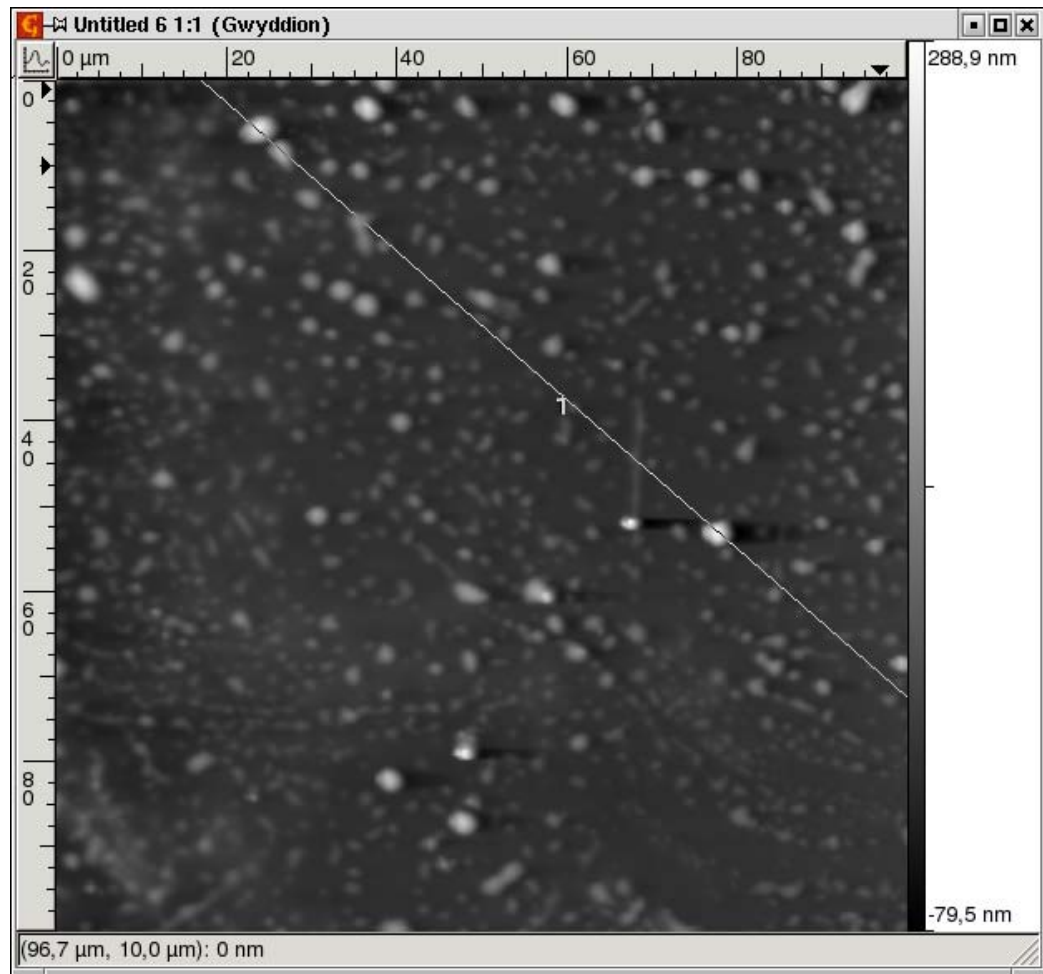
Figure 5.12: AFM picture of flatside of SIL.

above limit.

The third possible error is an air gap, or the distance **h** between a SIL and the sample. If the effective numerical apperture, NA_{eff}, is grater than 1 where $NA_{eff} = NA_{obj} \times n_{SIL}$, with NA_{obj} is numerical apperture of the objective 1/5 of the wavelength can deteriorate the resolution seriously. In our case, NA_{eff} is 2.04 with the values $NA_{obj} = 0.85$ and $n_{SIL} = 2.4$ [60].

To determine how big the air gap between the sample and the SIL is, surface charectarisation were done for the sample surface and the flat side of the SIL by using Atomic Force Microscope (AFM) (figures 5.12, 5.13, 5.14 and 5.15).
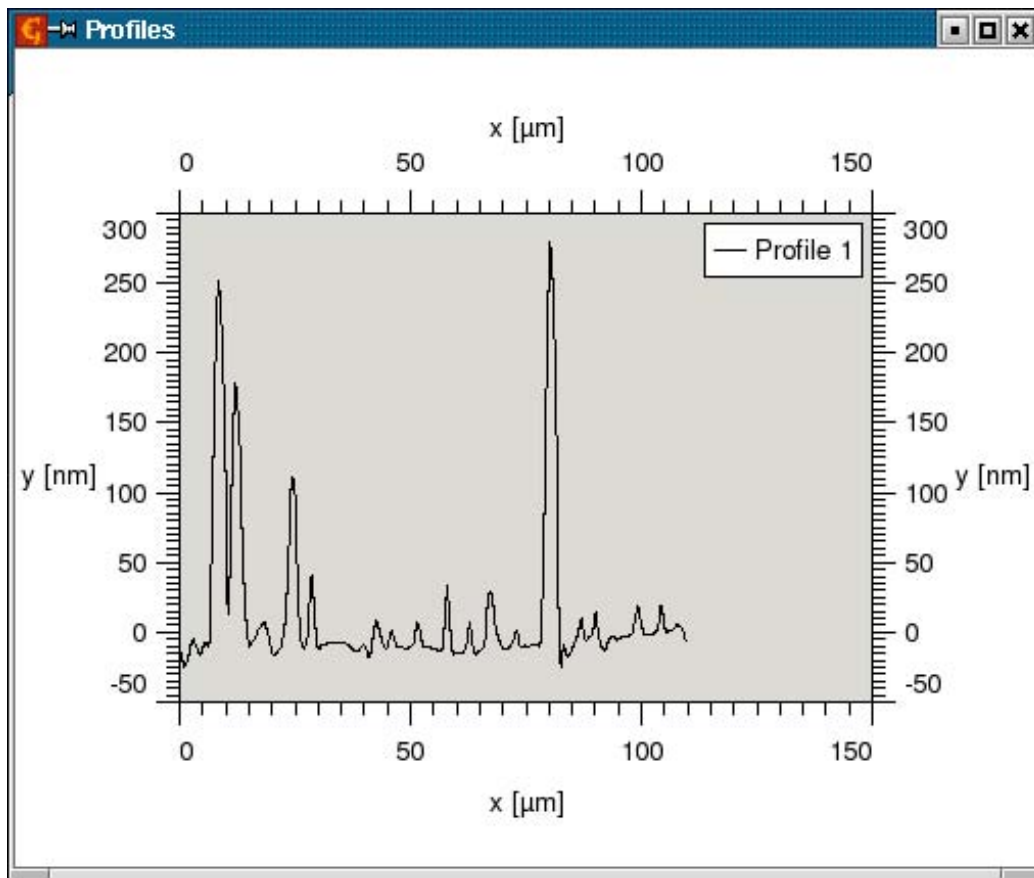
Figure 5.13: The height profile along the line shown in figure 5.12.
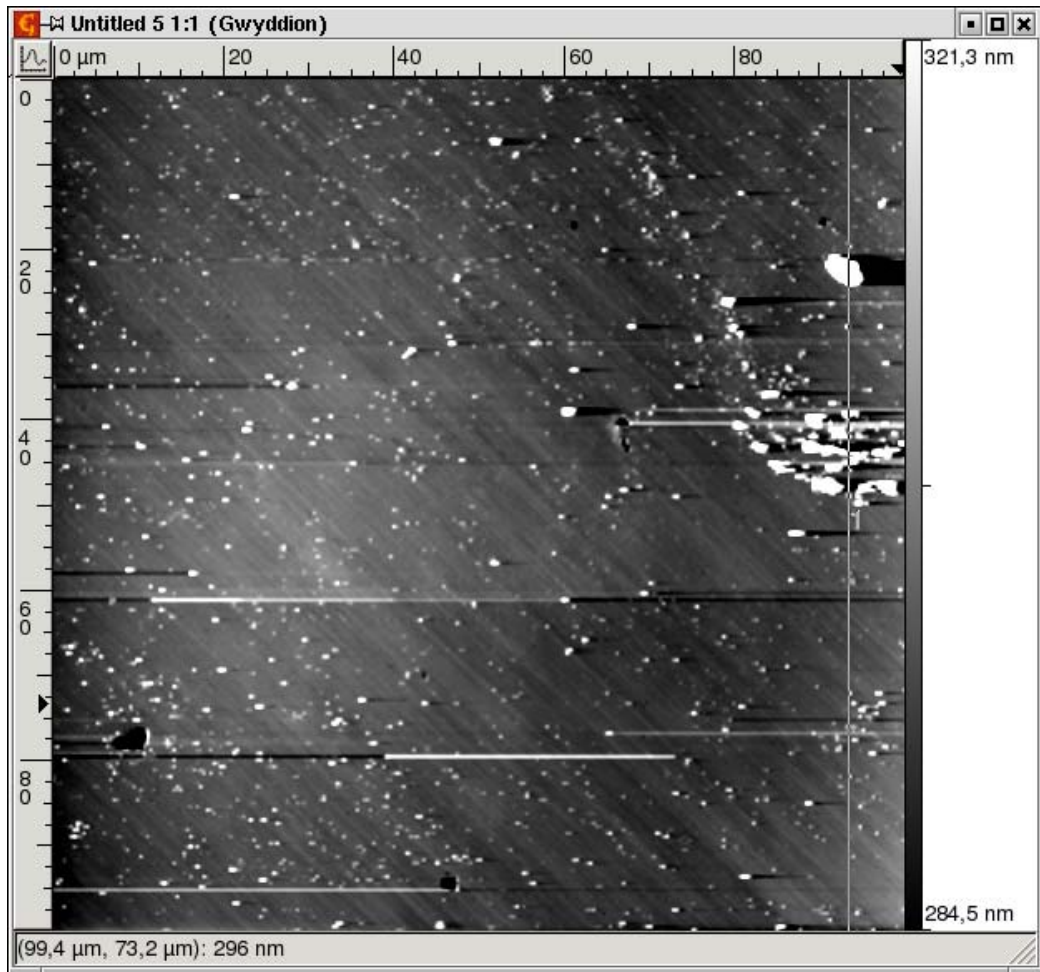
Figure 5.14: AFM picture of sample surface.
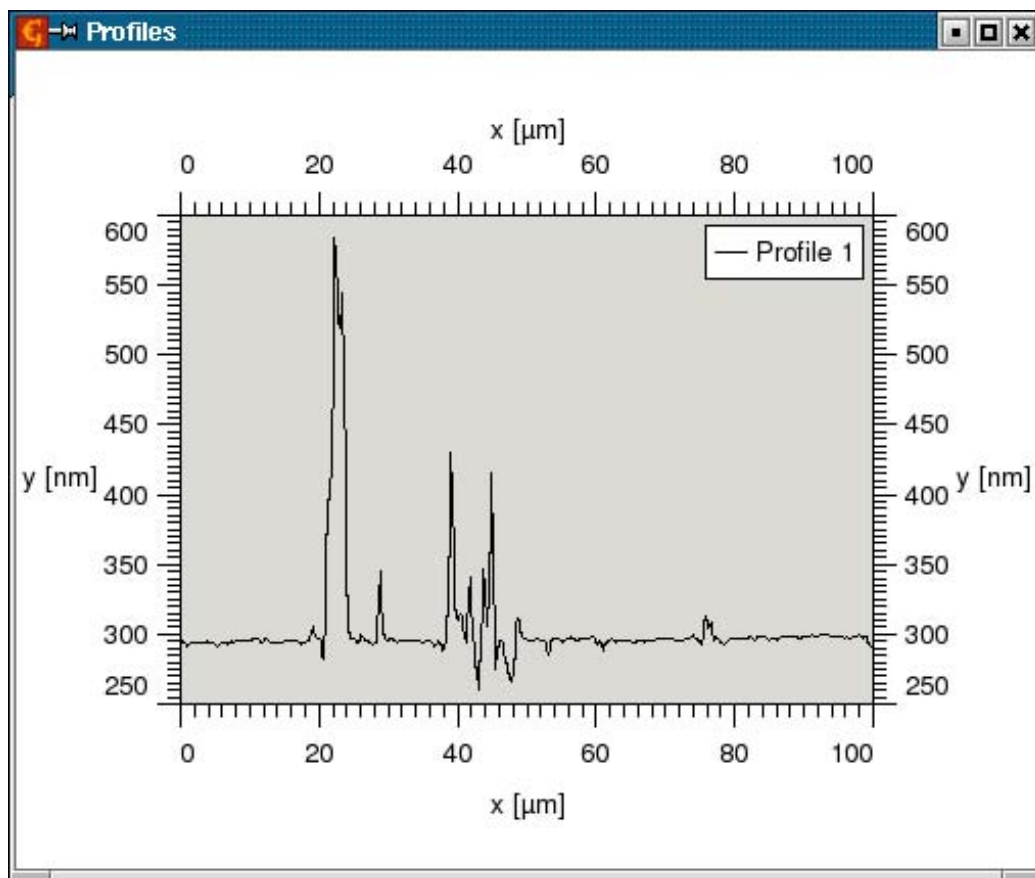
Figure 5.15: The height profile along the line shown in figure 5.14.

In AFM pictures some unknown structures can be seen in both surfaces. It is apparent that the airgap between the sample and SIL can be about 600 nm which is approximately one wavelength. This data tells us that the air gap can indeed influence our data.

The collection efficiency of a spectroscopy system is of crucial importance, especially in cases of low intensity excitation or low signal level. By comparing the luminescence intensities measured with SIL and without SIL, we find the enhancement of collection efficiency of our system using the SIL is up to ten times. For the case of an air gap of ≈ 600 nm, enhancement is only 1.5. The enhancement in collection efficiency is calculated by using the following formula $k_{total} = k_T \times k_\Omega$, where k_T and k_Ω are enhancement in transmission collection efficiency and solid angle collection efficieny ,respectively [60]. Since the n_{SIL} is larger than the refractive index of air the SIL has the property of reducing the reflection losses. The enhancement of the collection efficiency by this factor, k_T can be calculated by using the Fresnel formula, integrating over the whole solid angle. The SIL can enlarge the collection angle of the system. The solid angle outside the sample is independent of whether the SIL is used or not and is directly given by NA_{obj}. However the solid angle inside the sample increases when the SIL is introduced. This is due to the smaller reflection of light at the sample surface since the material on the top of the sample now has a refractive index higher than that of air. As a result light from a point source can be collected with a larger solid angle by the objective. The enhancement of collection efficiency due to the larger collection angle, k_Ω is given by the ratio of the solid angles.

Theoretically the calculated total collection efficiency should be ten times more with lens where the count rate should be 3700 counts/sec. We have 2146 counts/sec in the best case. With air gap the calculated value for the enhancement in collection efficiency is about 1.5, with a count rate of about 550 counts/sec, which is approximately in agreement with most of our SiV centers. From figure 5.8, the different count rates for different SiV centers can be seen. According to surface roughness of the SIL and sample we have different gap distances in each point. In the point where the higher count rate occurs, there is still an air gap which is small compared to other areas.

Chapter 6

Conclusions

This thesis was motivated by the idea to set up a single photon detection scheme in which a single silicon vacancy center in diamond acts as a single photon source. The production of silicon vacancy centers in diamond is achieved by ion implantation which allows uniform distribution of silicon vacancy centers. These centers act as a monolayer $2\mu m$ below the diamond surface. In our experiments, a single silicon vacancy centre acts as a stable single photon source with narrow emission spectrum at room temperature at 738 nm.

We applied the confocal microscope technique with the help of a solid immersion lense (SIL) to the microscopic photoluminescence spectroscopy of individual colour centers. The main benefits are improved resolution and collection efficiency. We demonstrated that the collection efficiency of the system with solid immersion lense in the best case is ≈ 6 times better than that of a conventional confocal microscope with a high numerical aperture objective.

We have discussed the possible errors which can occure when using solid immersion lenses: an aspheric error, a thickness error, and an air gap. The most important factor reducing the collection efficiency in our measurements is an air gap. According to the size of the air gap collection efficiency varies. In principle, the collection efficiency could be ten times higher than for the case without solid immersion lense.

We furthermore report on our room-temperature observation of single diamond color centers. Both, single-photon emission and metastable-state shelving are observed from photon time-correlation measurements with a Hanbury Brown and Twiss (HBT) setup. Due to the influence of nonra-

diative transitions, the single photon generation rate still needs some improvements, possibly by modifying the diamond environment. Together with high-Q cavities, high rate emission should be feasible, thereby enhancing the applicability of the silicon vacancy centres.

Bibliography

[1] R. Hanbury-Brown and R. Q. Twiss. A Test of a New Type of Stellar Interferometer on Sirius. *Nature*, 178:1046–1048, 1956.

[2] L. R. Walker J. P. Gordon and W. H. Louisell. Quantum Statistics of Masers and Attenuators. *Phys. Rev.*, 130:806–812, 1963.

[3] C.W. Gardiner and P. Zoller. *Quantum Noise*. Springer, (Berlin), 2000.

[4] Roy J. Glauber. The Quantum Theory of Optical Coherence. *Phys. Rev.*, 130:2529–2539, 1963.

[5] Roy J. Glauber. Coherent and Incoherent States of the Radiation Field. *Phys. Rev.*, 131:2766–2788, 1963.

[6] M. Dagenais H. J. Kimble and L. Mandel. Photon antibunching in resonance fluorescence. *Phys. Rev. Lett.*, 39:691–695, 1977.

[7] W. Tittel N. Gisin, G. Ribordy and H. Zbinden. Quantum cryptography. *Rev. Mod. Phys.*, 74:145–195, 2002.

[8] A. Ekert D. Bouwmeester and A. Zeilinger. *The Physics of Quantum Information*. Springer Verlag, (Berlin), 2000.

[9] W. K. Wootters and W. H. Zurek. A single quantum cannot be cloned. *Nature*, 299:802–803, 1982.

[10] C. H. Bennett and G. Brassard. Quantum Cryptography: Public Key Distribution and Coin Tossing. *Proceedings of IEEE International Conference on Computers Systems and Signal Processing, Bangalore India, December*, pages 175–179, 1984.

[11] Norbert Lutkenhaus. Security against individual attacks for realistic quantum key distribution. *Phys. Rev. A*, 61:052304–052313, 2000.

[12] A. Zeevi E. Waks and Y. Yamamoto. Security of quantum key distribution with entangled photons against individual attacks. *Phys. Rev. A*, 65:052310–052325, 2002.

[13] Norbert Lutkenhaus D. Gottesman, H.-K. Lo and John Preskill. Security of quantum key distribution with imperfect devices. *Quantum Information and Computation*, 4:325–360, 2004.

[14] W. Y. Hwang. Quantum Key Distribution with High Loss: Toward Global Secure Communication. *Phys. Rev. Lett.*, 91:057901–057904, 2003.

[15] Michael A. Nielsen and Isaac L. Chuang. *Quantum Computation and Quantum Information*. Cambridge University Press, (UK), 2000.

[16] W. E. Moerner. Single-photon sources based on single molecules in solids. *New J. Phys.*, 6:88, 2004.

[17] J-M Courty R Alleaume, F Treussart and J-F Roch. Photon statistics characterization of a single-photon source. *New J. Phys.*, 6:85, 2004.

[18] A. Kuhn M. Hennrich, T. Legero and G. Rempe. Photon statistics of a non-stationary periodically driven single-photon source. *New J. Phys.*, 6:86, 2004.

[19] K. Hayasaka W. Lange M. Keller, B. Lange and H. Walther. A calcium ion in a cavity as a controlled single-photon source. *New J. Phys.*, 6:95, 2004.

[20] P. Zarda C. Kurtsiefer, S. Mayer and H. Weinfurter. Stable solid-state source of single photons. *Phys. Rev. Lett.*, 85:290–293, 2000.

[21] R. Gacoin J. P. Poizat P. Grangier A. Beveratos, S. Kuhn. Room temperature stable single-photon source. *Eur. Phys. J. D*, 18:191–196, 2002.

[22] R. M. Stevenson A. J. Shields C. J. Lobo K. Cooper N. S. Beattie D. A. Ritchie M. Pepper Z. Yuan, B. E. Kardynal. Electrically Driven Single-Photon Source. *Science*, 295:102–105, 2002.

[23] J. Vuckovic G. S. Solomon C. Santori, D. Fattal and Y. Yamamoto. Single-photon generation with InAs quantum dots. *New J. Phys.*, 6:89, 2004.

[24] S. Tanzilli P. Baldi A. Beveratos N. Gisin S. Fasel, O. Alibart and H. Zbinden. High-quality asynchronous heralded single-photon source at telecom wavelength. *New J. Phys.*, 6:163, 2004.

[25] J. D. Franson T. B. Pittman, B. C. Jacobs. Heralding single photons from pulsed parametric down-conversion. *Opt. Comm.*, 246:545–550, 2005.

[26] F. Diedrich and H. Walther. Nonclassical radiation of a single stored ion. *Phys. Rev. Lett.*, 58:203–206, 1987.

[27] P. Michler et al. A quantum dot single-photon turnstile device. *Science*, 290:2282–2285, 2000.

[28] C. Santori et al. Triggered single photons from a quantum dot. *Phys. Rev. Lett.*, 86:1502–1505, 2001.

[29] P. Jonsson N. Panev S. Jeppsen T. Tsegaye E. Goobar M.-E. Pistol L. Samuelson V. Zwiller, H. Blom and G. Bjork. Single quantum dots emit single photons at a time: Antibunching experiments. *Appl. Phys. Lett.*, 78:2476–2478, 2001.

[30] C. Santori G. S. Solomon J. Vuckovic, D. Fattal and Y. Yamamoto. Enhanced single-photon emission from a quantum dot in a micropost microcavity. *Appl. Phys. Lett.*, 82:3596–3598, 2003.

[31] M. Orrit T. Bashe, W. E. Moerner and H. Talon. Photon antibunching in the fluorescence of a single dye molecule trapped in a solid. *Phys. Rev. Lett.*, 69:1516–1519, 1992.

[32] G. Zumofen B. Hecht L. Fleury, J.-M. Segura and U. P. Wild. Nonclassical photon statistics in single-molecule fluorescence at room temperature. *Phys. Rev. Lett.*, 84:1148–1151, 2000.

[33] J.-P. Poizat R. Brouri, A. Beveratos and P. Grangier. Photon antibunching in the fluorescence of individual color centers in diamond. *Opt. Lett.*, 25:1294–1296, 2000.

[34] Rodney Loudon. *The Quantum Theory of Light*. Oxford University Press, (USA), 2000.

[35] W. Lee. G. Goldhaber, S. Goldhaber and A. Pais. Influence of Bose-Einstein Statistics on the Antiproton-Proton Annihilation Process. *Phys. Rev.*, 120:300–312, 1960.

[36] M. Yasuda and F. Shimizu. Observation of Two-Atom Correlation of an Ultracold Neon Atomic Beam. *Phys. Rev. Lett.*, 77:3090–3093, 1996.

[37] M. Henny et al. The Fermionic Hanbury Brown and Twiss Experiment. *Science*, 284:296–298, 1999.

[38] R. C. Liu W. D. Oliver, J. Kim and Y. Yamamoto. Hanbury Brown and Twiss-Type Experiment with Electrons. *Science*, 284:299–301, 1999.

[39] Peter L. Knight. The Observation of Matter Wave Fluctuations. *Science*, 310:631–632, 2005.

[40] A. J. Bain and A. Squire. Super-Gaussian field statistics in broadband laser emission. *Opt. Commun.*, 135:157–163, 1997.

[41] Charles Kittel. *Introduction to Solid State Physics - 7th ed.* John Wiley & Sons, (Canada), 1996.

[42] A. M. Zaitsev. Vibronic spectra of impurity-related optical centers in diamond. *Phys. Rev B*, 61:12909–12922, 2000.

[43] B. V. Zaitsev B. V. Deryagin B. V. Spitsyn V. S. Vavilov, A. A. Gippius and A. E. Aleksenko. . *Sov. Phys. Semicond.*, 14:1078, 1980.

[44] I. Kiflawi C. D. Clark, H. Kanda and G. Sittas. Silicon defects in diamond. *Phys. Rev. B*, 51:1668116688, 1995.

[45] S. W. Brown and S. C. Rand. Site symmetry analysis of the 738 nm defect in diamond. *J. Appl. Phys.*, 78:4069–4075, 1995.

[46] S. J. Breuer P. R. Briddon J. P. Goss, R. Jones and S. Öberg. The Twelve-Line 1.682 eV Luminescence Center in Diamond and the Vacancy-Silicon Complex. *Phys. Rev. Lett.*, 77:30413044, 1996.

[47] Chunlang Wang. Festkörperbasierte einzelphotonenquelle, 2003.

[48] W. J. Choyke J. Ruan and W. D. Partlow. Si impurity in chemical vapor deposited diamond films. *Appl. Phys. Lett.*, 58:295–297, 1990.

[49] R. Sauer P. C. Münzinger H. Sternschulte, K. Thonke and P. Michler. 1.681-eV luminescence center in chemical-vapor-deposited homoepitaxial diamond films. *Phys. Rev. B*, 50:1455414560, 1994.

[50] Nugent K. W. Robertson J. Sands H. S. Lifshitz Y. Shi X. Gilkes K. W. R., Prawer S. . *J. Appl. Phys.*, 80:7823, 2000.

[51] M. Baba M. Yoshita, T. Sasaki and H. Akiyama. Application of solid immersion lens to high-spatial resolution photoluminescence imaging of GaAs quantum wells at low temperatures. *Appl. Phys. Lett.*, 73:635–637, 1998.

[52] M. Baba T. Suemoto K. Koyama, M. Yoshita and H. Akiyama. High collection efficiency in fluorescence microscopy with a solid immersion lens. *Appl. Phys. Lett.*, 75:1667–1669, 1999.

[53] M. Born and E. Wolf. *Principles of Optics, 7th ed.* Cambridge University Press, (Cambridge), 1999.

[54] M. Orrit T. Basche, W. E. Moerner and U. P. Wild. *Principles of Optics, 7th ed.* VCH Publishers, (Cambridge), 1996.

[55] F. Bloch. Nuclear Induction. *Phys. Rev.*, 70:460474, 1946.

[56] J. Rarity S. Kitson, P. Jonsson and P. Tapster. Intensity fluctuation spectroscopy of small number of dye molecules in a microcavity. *Phys. Rev. A*, 58:620–627, 1998.

[57] J. Wrachtrup and F. Jelezko. Processing quantum information in diamond. *J. Phys. Cond. Mat.*, 18:807–824, 2006.

[58] C. Tietz F. Jelezko S. Kilin A. Nizovtev A. Drabenstedt, L. Fleury and J. Wrachtrup. Low-temperature microscopy and spectroscopy on single defect centers in diamond. *Phys. Rev. B*, 60:1150311508, 1999.

[59] Masahiro Yoshita Motoyoshi Baba, Takeaki Sasaki and Hidefumi Akiyama. Aberrations and allowances for errors in a hemisphere solid immersion lens for submicron-resolution photoluminescence microscopy. *J. Appl. Phys.*, 85:6923–6925, 1999.

[60] B. Dal Don S. Wachter S. Moehl, H. Zhoi and H. Kalt. Solid immersion lens-enhanced nano-photoluminescence: Principle and applications. *J. Appl. Phys.*, 93:6265–6272, 2003.

List of Tables

List of Figures

Acknowledgements

Erklärung

des Studierenden im Masterstudiengang Engineering Physics

Name:

Vorname:

Mit der Abgabe der Master Thesis versichere ich, dass ich die Arbeit selbständig
verfasst und keine anderen als die angegebenen Quellen und Hilfsmittel benutzt habe.

....
(Ort, Datum)

....
(Unterschrift)